Characterizing Aerodynamics and Flutter Behavior of Flags in a Free Jet Flow

A Thesis

Presented in Partial Fulfillment of the Requirements for the

Degree of Master of Science

with a

Major in Mechanical Engineering

in the

College of Graduate Studies

University of Idaho

by

Rodrigo Padilla

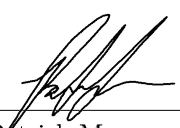Major Professor: Vibhav Durgesh, Ph.D.

Committee Members: Tao Xing, Ph.D.; Gabriel Potirniche, Ph.D.; Patrick Musgrave, Ph.D.

Department Administrator: Gabriel Potirniche, Ph.D.

August 2021

AUTHORIZATION TO SUBMIT THESIS

This thesis of Rodrigo Padilla, submitted for the degree of Master of Science with a Major in Mechanical Engineering and titled "Characterizing Aerodynamics and Flutter Behavior of Flags in a Free Jet Flow," has been reviewed in final form. Permission, as indicated by the signatures and dates below is now granted to submit final copies for the College of Graduate Studies for approval.

Advisor: _____ 08/05/2021
Vibhav Durgesh, Ph.D.   Date

Committee Members: _____ 8/5/2021
Tao Xing, Ph.D.   Date

_____ 8/5/2021
Gabriel Potirniche, Ph.D.   Date

_____ 08/04/2021
Patrick Musgrave, Ph.D.   Date

Department Chair: _____ 8/5/2021
Gabriel Potirniche, Ph.D.   Date

Abstract

Fluid-Structure Interactions (FSI) is a widely studied area of research in the field of fluid dynamics since a detailed understanding of FSI flow behavior can impact a wide range of engineering applications like new generation parachutes used in space exploration, helicopter aerodynamics, bio-propulsion, and flexible wing aerodynamics. However, developing a detailed understanding of the underlying physics in an FSI flow can be challenging due to the non-linear nature of the coupling between fluid flow and structures. Therefore, this investigation aims to quantify the FSI behavior of a flag in uniform jet flow, specifically the flutter movement, aerodynamic performance, and fluid flow velocity field around the flag. For this purpose, three flag samples of varying lengths were used, and experiments were performed for a range of three critical non-dimensional parameters, i.e., Mass Ratio (R_1), Dimensionless Rigidity (R_2), and Reynolds number (Re). The R_1 and R_2 values were varied from 1.48 to 2.77, and 1.3×10^{-3} to 14.4×10^{-3}, respectively, and Reynolds Number was varied from 44×10^3 to 123×10^3. All experiments were conducted in the subsonic open jet facility at the University of Idaho's Experimental Fluids and Aerodynamics Laboratory. The aerodynamic load experienced by the flag was measured using a high-precision load cell. The flag movement was captured using a triggered image acquisition system, and Particle Image Velocimetry (PIV) was used to measure the velocity fields around the fluttering flag. The results showed that the longest flag model has a unique aerodynamic load characteristic, i.e., a drag crisis region for R_2 from 3.1×10^{-3} to 5.3×10^{-3} followed by a drag recovery region for R_2 from 1.9×10^{-3} to 3.1×10^{-3}. All the studied flag models start oscillating with increasing Re at a critical velocity and initially exhibit mode-2 oscillation behavior. With the further increase in Re, the longest flag model transitions from mode-2 to a mode-3 oscillation. Furthermore, these results suggest that the flag movement and oscillation modes contribute to observed drag by these models. Finally, the stability plots identify a new region highlighting the transition from mode-2 to mode-3 oscillation behavior.

Acknowledgements

DEDICATION

For my mom Guadalupe Rodriguez-Rosas, my dad Rodrigo Padilla, my sisters Jeanette Padilla and

Elizabeth Padilla, and my friends who have given me all their love and support.

TABLE OF CONTENTS

List of Tables

List of Figures

List of Acronyms

A_r reference area (m^2)

AR aspect ratio

A_1 amplitude of oscillation (mm)

A_L amplitude of oscillation normalized by flag length

A_2 second amplitude of oscillation (mm)

C_D drag coefficient

C_L lift coefficient

D bending rigidity

D_1 jet diameter (mm)

D_2 stand diameter (mm)

E young's modulus (GPa)

FSI   fluid-structure interactions

L flag length (mm)

$\hat{n}$ normal unit vector

N_e amplitude of neck (mm)

p pressure (Pa)

PIV   particle image velocimetry

R_1 mass ratio

R_2 dimensionless rigidity

Re Reynolds number

s curvilinear coordinates of the flag

St_{A_1} Strouhal number based on amplitude of oscillation

St_L Strouhal number based on length

T tension force (N)

h flag thickness (mm)

U_x x component of inlet velocity (m/s)

U_y y component of inlet velocity (m/s)

U_c lower critical velocity (m/s)

U_d higher critical velocity (m/s)

U_∞ inlet velocity (m/s)

w flag width (mm)

$\mathbf{X}$ vector of flag displacement

$\mathbf{RPM}$ electro-craft control knob value (rotational)

ρ_f density of the fluid (kg/m^3)

ρ_s density of the structure (kg/m^3)

β fluid damping coefficient

ζ internal damping coefficient

μ dynamic viscosity (kg/ms)

Chapter 1: Introduction

Fluid-Structure Interactions (FSI) is the coupling between a flowing fluid with a structure that results in either a static or dynamic deformation of the structure, and the deformation could be either small or large. This fluid-structure interactions (FSI) behavior is observed in daily experiences such as a leaf falling off a tree, a sail on a boat, an airplane wing subjected to flutter by fluid loading, an animal's flexible body used for propulsion, and a flag fluttering in the wind. However, due to the non-linear nature of the problem, there is yet to be any closed-form analytical solution. For this reason, idealized models are often used to understand the underlying physics of the FSI behavior for both computational and experimental investigations.

One such idealized model that captures the complex FSI behavior is the fluttering of a flag, which has been extensively studied both experimentally [Taneda, 1968, Virot et al., 2013, Watanabe et al., 2002] and numerically [Argentina and Mahadevan, 2005, Eloy et al., 2007]. The idealized flag reduces the FSI behavior to desirable and controllable parameters while retaining non-linearities of the system and the multi-physics complexities. In attempts to understand the flag problem, experiments have been conducted in either a wind tunnel [Eloy et al., 2008, Gibbs et al., 2014, Taneda, 1968], free jet [Lemaitre et al., 2005], or water tunnel [Jia et al., 2018, Shelley et al., 2005]. These studies have highlighted the key parameters that influence the FSI behavior which is the flow velocity, the pressure acting normal to the flag, viscosity, density, flag geometry, Young's Modulus, and bending stiffness. These parameters will be the variables used to quantify the non-dimensional terms. In these studies, the researchers have observed two states of flag oscillations 1) the straight state and 2) flutter state [Taneda, 1968]. The straight state will have small-scale vibration, while the flutter will have large-scale deformations. In recent studies, Alben and Shelley have developed a stability boundary for the flag with a range of critical non-dimensional parameters [Alben and Shelley, 2008]. Moreover, conducting experiments is challenging due to the non-linear nature of the interaction; the flag response is sensitive to the initial boundary conditions and any instabilities in the fluid.

The FSI flag problem can be further classified into three categories based on their arrangements. The first being the standard flag [Alben and Shelley, 2008, Taneda, 1968, Watanabe et al., 2002], the second is the inverted flag [Kim et al., 2013, Tang et al., 2015, Yu et al., 2017], and the third is the flag in the wake of a bluff body [Pan et al., 2014, Shi et al., 2013, Yu and Liu, 2015]. Figure 1.1, shows the configuration of all three flag types. While all three flag types share the same governing equations and parameters, each will have different boundary conditions and a different flutter behavior. Due to the configuration used in this thesis emphasis is placed on the standard flag.

Taneda[Taneda, 1968] was the first to study the standard flag and quantified the flutter behavior using various materials. His study showed a linearly increasing flutter frequency of the flag with an increasing inlet velocity, U_∞. Following Taneda's work, several researchers studied the FSI standard flag problem. Some of the crucial observations from these studies is the existence of two critical velocities bounded with a hysteresis loop [Watanabe et al., 2002], change in flutter behavior with changing in the inflow condition [Shelley et al., 2005], and growth in the amplitude of oscillation will also lead to higher drag values experienced at higher Re [Virot et al., 2013]. While several aerodynamic measurements have been done for the various flutter behavior and earlier studies have provided a better insight into the FSI physics, there are still several unknowns. Therefore, a better understanding of FSI can impact industries such as aerospace, bio-propulsion, and energy harvesting. Understanding the complex flag motion can translate to applications such as the wings of aircraft which are susceptible to flutter [Bottai et al., 2019], or vibrations of panels in aircrafts [Dowell, 1970]. Considering both scenarios having a higher structural stiffness, understanding the more complex flag problem can aid in their design and modeling. Another area where the FSI physics will have an impact is in the fields of bio-propulsion and flight, such as fishes using their flexible bodies to generate a thrust [Sfakiotakis et al., 1999]. While birds and insects use their flapping wings to propel through the air [Dhawan, 1991, Sane, 2003]. Finally, the FSI flag problem can be applied to energy harvesting [Giacomello and Porfiri, 2011, Li and Lipson, 2009] and passive heat transfer [Gallegos and Sharma, 2017, Herrault et al., 2012].
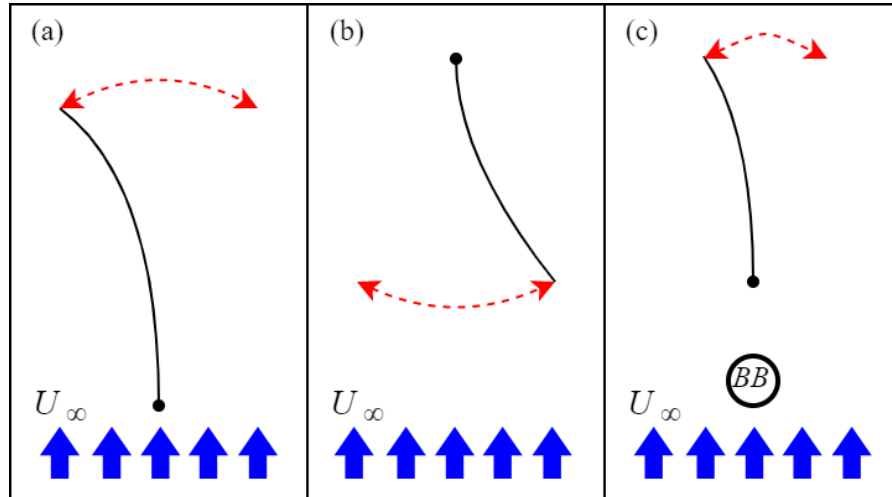
Figure 1.1: The three types of flag configurations: a) standard flag with a fixed leading edge and free trailing edge, b) inverted flag with a free leading edge and fixed trailing edge, and c) standard or inverted flag in the wake of a bluff body.

1.1 OBJECTIVE

To understand the standard flag's oscillation modes, its dynamics, and impact of fluid flow on the aerodynamics response, selected non-dimensional parameters were chosen based on the boundary stability of the flag. The R_1 was selected such that the region of mode-2 could be spanned. Furthermore, the non-dimensional parameters R_2 and R_2 were dictated based on the selected R_1 as well as the complete range of inlet velocities possible by the jet facility. Moreover, the three main objectives chosen for this study are as follows:

1. Quantify aerodynamic behavior for the fluttering of the flag for critical non-dimensional parameters mass ratio (R_1), dimensionless rigidity (R_2), Reynolds number (Re) with the values of $44,000 - 123,000$, $1.48 - 2.77$, and $1.3 \times 10^{-3} - 14.5 \times 10^{-3}$, respectively.

2. Quantify the dynamic load characteristic for the studied flag models for the range of non-dimensional parameters.

3. Quantify flutter shapes and velocity for mode-2 and mode-3 oscillation observed for the studied flags.

Different flag samples were used to achieve these objectives, and an in-house free jet was operated to control the inflow conditions. Aerodynamics loads, flag positions, and velocity flow fields were measured. The aerodynamics load data was analyzed to identify the dominant frequency. Flag images were used to identify flutter characteristics. A particle image velocimetry (PIV) system was used to capture the flag flutter along with the velocity field of the surrounding fluid. The results showed a flag flutter is dependent on the three critical non-dimensional parameters R_1, R_2, and Re, aerodynamics loads vary with the oscillation modes, and there is a correlation between the oscillation modes and the observed dominant frequencies.

The following section provides an extensive background study, in chapter 2, on the topic of the flag problem that will cover experimental and computational studies—followed by the detailed experimental setup and procedure, chapter 3. Including a discussion on the samples selected, detail on the load cell used to measure aerodynamic loads, and detail on the PIV used to quantify the flow field. Uncertainties related to the study are also presented, chapter 4. The final section includes a discussion in chapter 6 on the results, followed by a summary and conclusion of the results, chapter 7.

Chapter 2: Background Study

2.1 Governing Equations

Governing equations for the FSI flag problem configurations are defined by the same equations but with varying boundary and initial conditions. The fluid is governed by the incompressible viscous form of the Navier-Stokes equations with the continuity equation 2.1 and momentum equation 2.2 shown as follows,

$$\nabla \cdot \mathbf{u} \quad = \quad 0, \quad \text{and} \tag{2.1}$$

$$\frac{\partial \mathbf{u}}{\partial x} + (\mathbf{u} \cdot \nabla) \mathbf{u} \quad = \quad -\frac{1}{\rho_f} (\nabla p) + \nu \nabla^2 \mathbf{u}, \quad \text{respectively,} \tag{2.2}$$

$$\text{where,} \quad \mathbf{u} \quad = \quad \frac{\partial \mathbf{X}}{\partial t}, \tag{2.3}$$

$\mathbf{u}$ is the fluid velocity, ρ_f is the fluid density, p is the pressure of the fluid, and μ is the dynamic viscosity. The fluid forces that are acting on the standard flag and the response are shown in figure 2.1. Furthermore, newton's second law can be used to derivative the governing equation based on the initial assumptions for the equation of motion for the deforming flag. The following equation 2.4 can be derived [Païdoussis, 1998],

$$D\frac{\partial^4 X}{\partial s^4} + \rho_s h \frac{\partial^2 \mathbf{X}}{\partial t^2} - \frac{\partial}{\partial s} \left(T \frac{\partial \mathbf{X}}{\partial s} \right) + \beta \frac{\partial \mathbf{X}}{\partial t} + \zeta \frac{\partial}{\partial t} \left(\frac{\partial^4 \mathbf{X}}{\partial s^4} \right) = \delta \mathbf{p} \hat{n}. \tag{2.4}$$

The term s is the curvilinear coordinate and is related to the vector as $\mathbf{X} = (X(s,t), Y(s,t))$ which is the displacement of the flag from it's mean position. D is the flags bending rigidity, ρ_s is the density of the flag, and h is the thickness of the flag. T is the tension force along the tangential direction of the flag. The terms β and ζ are associated with the flags, fluid damping coefficient due to the fluid's viscosity, and internal damping coefficient due to the structural damping, respectively. There is a pressure differential normal unit vector $(\hat{n})$ to the faces of the flag shown as ∇p. There are variations of this equation such that some terms will neglect based on the initial assumption of the problem.

2.2 Flag Problem

Since the governing equations do not have a direct solution, this motivates researchers to conduct controlled experimental comprehend the observed phenomenons. Some of the unique phenomena that
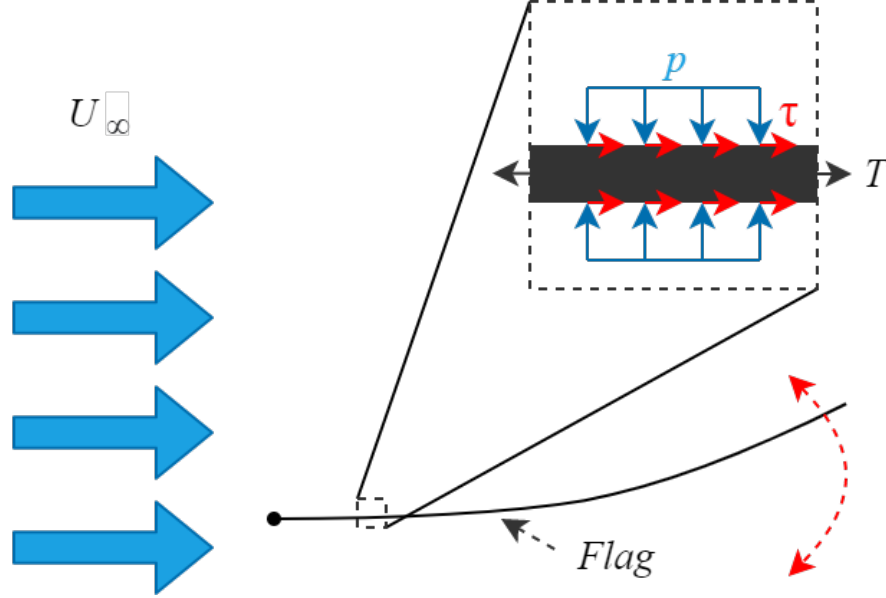
Figure 2.1: View of the fluid forces acting on a standard flag while in fluttering motion.

have been reported through researched theories are the boundary stability based on the non-dimensional variables that contain the small bifurcation region at the point where stability is lost [Alben and Shelley, 2008, Eloy et al., 2012, Tang et al., 2007, Watanabe et al., 2002, Zhang et al., 2000]. Sudden increases in drag have been documented when flutter is induced [Carruthers and Filippone, 2005, Fairthorne, 1930, Lemaitre et al., 2005, Morris-Thomas and Steen, 2009, Virot et al., 2013]. With the term flutter referring to the act of a flags motioning which exhibits large displacements. Flutter occurs due to the instability in the fluid loading causing an oscillatory behavior [Argentina and Mahadevan, 2005]. During oscillatory motion, various flutter modes at varying non-dimensional parameters have been documented [Eloy et al., 2008, Taneda, 1968, Virot et al., 2013]. Furthermore, oscillations cause a change in the vortex generation downstream of the flag for the various states and modes [Taneda, 1968, Zhang et al., 2000, Virot et al., 2013].

The mentioned phenomenon are influenced by the flag's and fluid's properties. Leading several researchers to employ wind tunnel studies to mimic inflow conditions [Carruthers and Filippone, 2005, Chun-Yu et al., 2010, Eloy et al., 2012, Fairthorne, 1930, Gibbs et al., 2014, Kim et al., 2013, Lemaitre et al., 2005, Huang, 1995, Morris-Thomas and Steen, 2009, Pang et al., 2010, Tang et al., 2003, Taneda, 1968, Virot et al., 2013, Watanabe et al., 2002], in which ambient air is the fluid source. It is desirable to have controllable conditions such as the inlet fluid source with ranging velocities and a test section with optical access. Though it is vital to understand that there exist inherent effects of wind tunnel testing, such as the placement of the specimen. The fluttering flag experiences large displacement that

can cause dynamic blockage effects [Tang et al., 2007]. As reported in the review paper on "Fluid-Induced Flag Vibrations," the maximum amplitude displacement could be 80% of the flag length from the center-line of a flag at rest [Yu et al., 2019]. Though the amount of displacement depends on the type of flag configuration selected to be studied, but for all configurations' it is significant enough where blockage effects should be considered.

The three flag configurations are a standard flag, an inverted flag, and a flag behind the bluff body, as shown in Figure 1.1. The standard flag, which is the configuration being tested in this study, is fixed at the upstream position. This fixed edge allows the flag to be parallel with the flow at lower or stabilizing velocities. Upon reaching the critical velocity, U_d, which varies based on flag and fluid properties [Watanabe et al., 2002], an onset flutter is experienced that impacts the aerodynamics. When the fluid velocity is lowered, the flag remains in a fluttering state until a lower speed is reached, which is called the lower critical velocity, U_c. At this second critical velocity, the flag will go back to a straight state. Within the range of critical velocities, the flag could be in a straight state or a flutter state and has been referred to as bifurcation, or hysteresis loop [Alben and Shelley, 2008, Eloy et al., 2012, Tang et al., 2007, Watanabe et al., 2002, Zhang et al., 2000]. Due to the low stiffness rigidity at critical velocities, the free end, which is at the downstream position, begins experiencing large displacement. The maximum distance displaced will be referred to as the amplitude of oscillation, A_1, which is measurable by quantifying the tip to tip displacement experienced in the flutter cycle.

For an inverted flag, the configuration is reversed as the fixed edge is downstream. The free edge is located upstream and can remain in a straight state at lower velocities. Similar to the standard flag, the bifurcation region exists with the two critical velocities, critical velocity, U_d, and lower critical velocity, U_c, with the ability to be in either a straight state or flutter state [Kim et al., 2013]. At the critical velocity, U_d, the flutter behavior will be that as shown in Figure 3.4(b). The flutter deflection can also be quantified by measuring the maximum displacement, also denoted by A_1. A second change in behavior and bifurcation region at a higher velocity also exists such that the inverted flag can exist in a flutter state or a deflected state. The deflected state is also visually distinct as it does not exhibit fluttering motion but instead is held at one extreme due to fluid loading.

The final configuration is the flag behind the bluff body which could be either a standard flag or an inverted flag. The bluff body could be of various geometries such as a square bluff body [Pan et al., 2014, Shi et al., 2013], a circular bluff body [Yu and Liu, 2015], or another shape. Extensive understanding and reviews of bluff bodies are available that show vortex shedding of various geometry in axial flow [Sarpkaya, 1979]. The final configuration flag is located in the wake of the bluff body. The bluff body will change the fluid loading on the flag and will induce flutter before the known critical

velocities [Kim et al., 2013].

Since the current thesis paper is on the standard flag, the focus is placed on the current known knowledge of this configuration. Background is given on the following phenomenons have been studied with the use of experimental means to use non-dimensional values to characterize flutter behavior [Alben and Shelley, 2008, Argentina and Mahadevan, 2005, Eloy et al., 2007], quantifying the flag motion employing imaging techniques [Taneda, 1968, Virot et al., 2013, Pang et al., 2010], measurements of the aerodynamics loads generated due to the flag motion [Carruthers and Filippone, 2005, Fairthorne, 1930], or quantifying the near-wall velocity fluid field with PIV [Gibbs et al., 2014, Jia et al., 2007]. Though various controllable parameters play a key role in the resulting outcome of the standard flag. These key parameters can be non-dimensionalized into key equations that are best used to analyze the flag problem. The non-dimensional terms selected to be used in this paper to understand the flag problem are the mass ratio (R_1), dimensionless rigidity (R_2), Reynolds number (Re), drag coefficient (C_D), and aspect ratio (AR). With there respective equations are as follows:

$$R_1 = \frac{\rho_m h}{\rho_f L}, \tag{2.5}$$

$$R_2 = \frac{E t^3}{12\left(1 - \nu^2\right)\rho_f U_\infty^2 L^3}, \tag{2.6}$$

$$Re = \frac{\rho_f U_\infty L}{\mu}, \tag{2.7}$$

$$C_D = \frac{F_D}{\frac{1}{2}\rho_f U_\infty^2 A_r}, and \tag{2.8}$$

$$AR = \frac{w}{L}. \tag{2.9}$$

The terms in the equations are the inlet velocity (m/s) (U_∞), density of the fluid (kg/m^3) (ρ_f), density of the structure (kg/m^3) (ρ_s), dynamic viscosity (kg/ms) (μ), young's modulus (GPa) (E), flag length (mm) (L), flag thickness (mm) (h), and reference area (m^2) (A_r). R_2 as a function of R_1 is used to define the stability boundary which shows where the flag will either be in a straight state or have onset flutter. Recent work on stability of the flag has been summarized on the review of the flag problem [Yu et al., 2019], presented in Figure 2.2. Included text in the figure are IIE, EIE, and MIE which are annotations for the inverted flag, bluff body with the flag in the wake, and standard flag, respectively. Numerical studies have aimed to generate a function that will define the boundary stability that will predict flutter behavior but has yet to be properly captured. Furthermore, current attempts have only qualitatively captured the trend seen in experimental data [Alben and Shelley, 2008, Eloy et al., 2008].

For this reason, based on experimental results a grey-shaded area in the figure is defined to show the general region where the standard flag has been unstable and will be fluttering. The white region will be the stable area where the flag will not flutter. If the material properties of the flag and fluid were to remain constant, with the only varying condition be the ,U_∞, the only varying term in the stability boundary will be R_2. Furthermore, all flag scenarios with small U_∞ that result in a $R_2 \geq 1$ will not experience flutter motion. As U_∞ is increasing R_2 is decreasing, until the defined lower critical velocity (m/s) (U_c) and higher critical velocity (m/s) (U_d) is reach which causes instability about the transition line that will lead into the unstable grey region. The point of onset flutter is dictated by the matching R_2 value at the corresponding R_1.
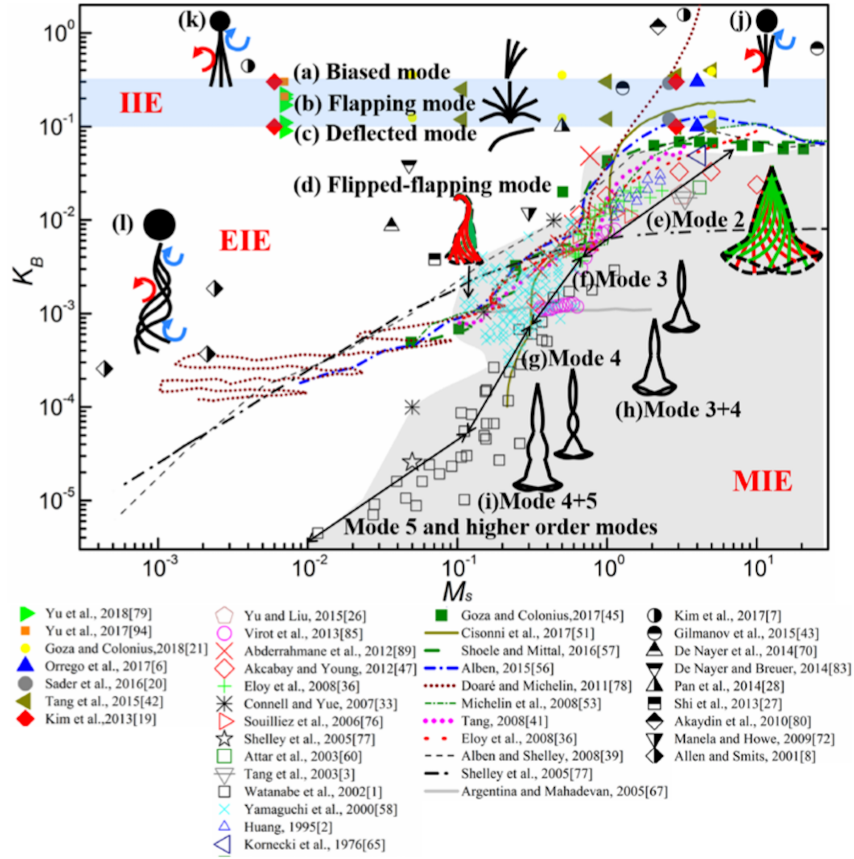
Figure 2.2: The summarized boundary stability for various prior studies [Yu et al., 2019]; K_B is the dimensionless rigidity (R_2) and M_s is the mass ratio (R_1). IIE being the inverted flag, EIE being the flag in the wake of a bluff body, and MIE is the standard flags. Regions are generally indicated for each type.

Additionally, the stability boundary can distinguish what flutter mode will initially be experienced by the flag upon onset flutter. The various flutter modes have been defined by the dominant vibration modes of the cantilevered beam in a vacuum. Modes are associated with the eigenvalues of the system,

which are used to analyze the stability of the flag [Eloy et al., 2007]. Due to the nature of eigenvalue problems n number of vibration modes are possible, where $n = 1, 2, 3, ...\infty$. For this reason, only the initial vibration modes are mentioned. Furthermore, researchers named flutter mode depending on the current dominant vibration mode, n. An example is "mode-1 vibration," which will have a simple swaying motion that does not have a large displacement and is an attribute of the flag in a straight state. For this reason, large displacements begin at a mode-2 or higher flutter type. The shape of the flutter is defined by the superimposition of a complete limit cycle, complete harmonic motion of the flutter flag, which has definable characteristics based on the mode. Included at the amplitude of oscillation A_1, defined as the maximum displacement experienced by the flag. Moreover, for mode-2 flutter the A_1 is known to increase with the increase of the flow velocity [Chun-Yu et al., 2010, Eloy et al., 2008]. A neck amplitude of neck (mm) (N_e) is also defined as regions where flutter amplitude is locally smaller [Virot et al., 2013].

The shape for flutter modes are is shown in Figure 2.2 to the right of each text, e.g. next to "(e) Mode 2" the mode-2 flutter with the fixed edge at the top portion of the shape is shown. In Figure 2.2, a mass ratio range can be defined on the grey region on the stability boundary that will exhibit specific flutter modes for the standard flag. For flags scenarios with a $R_1 \geq 0.7$, mode-2 flutter will be initially experienced [Eloy et al., 2007]. Followings mode-2 will be the mode-3 flutter with the mass ratio bounded by $0.3 \leq R_1 \leq 0.7$, shown in the Figure 2.2 to the right of the text "(f) Mode 3". Higher flutter modes will be at values for $R_1 \leq 0.3$ and will experience unique flutter behavior. On the other hand, few studies have documented mode shape changes as R_2 is decreased [Chen et al., 2014, Virot et al., 2013]. These cases begin with a flutter mode-2 that will transition into a mode-3 with a decreasing R_2. Though this will not be experienced for all scenarios since some flags will go from a mode-2 to a chaotic flutter [Connell and Yue, 2007, Shelley et al., 2005], with chaotic flutter classified as random displacement without a coherent shape. The regions of R_1 to which modal changes apply are yet to be defined. While chaotic is always experienced after the maximum amplitude is reached [Shelley et al., 2005] and is yet to be understood properly.

Different conditions will apply to the infinite flag problem (infinitely thin flags); an infinite long flag will always be unstable, and a flag with infinite span will need a substantial velocity to destabilize [Eloy et al., 2007]. For a finite flag, it has been shown that the short flag will have a higher U_c as opposed to longer flags, and as the length is increased, the U_c will rapidly decrease. For longer flags, the dependency on varying lengths is seen to be weak since, after a certain critical length, the U_c remains constant [Lemaitre et al., 2005]. If the inlet velocity is kept constant and a single geometric property is varied, in this case, the length, the flag can experience a variation of the previously mentioned

bifurcation. It is different such that there will be two critical lengths in which flutter can be stable or unstable [Zhang et al., 2000] with shorter flags remaining stable and large always being unstable. The mass ratio was also varied by changing the material property that will affect the density of the structure. Changing structural density is seen to comply with the stability boundary, which will require a higher critical velocity for a denser material [Watanabe et al., 2002].

The suddenly induced flutter of the flag has a change in aerodynamics that is experienced. In a straight state, the flag will experience a decrease in C_D with the increasing wind velocity and Reynolds number [Carruthers and Filippone, 2005]. Changing material will also change the y-intercept of the C_D. The variation of geometry and flow conditions will impact the drag experienced for a flag in straights state [Fairthorne, 1930]. Once the flag begins to flutter, a sudden spike in drag is experienced [Taneda, 1968]. The aerodynamics is further studied for scenarios that will experience modal changes, with the introduction of the drag crisis region where the C_D will begin to decrease at the velocity increases [Carruthers and Filippone, 2005].

From the oscillatory behavior of the fluttering flag, a dominant frequency can be defined. With the increase of the velocity, a linear relationship with the flutter frequency is observed [Taneda, 1968]. In figure 2.3, Taneda further demonstrates that when the material property is varied, the slope of the linear relationship will change. These values can be non-dimensionalized to acquire the Strouhal number based on amplitude of oscillation (St_{A_1}) and Strouhal number based on length (St_L). The results of various studies have been summarized to result in a linear relationship between the St_{A_1} as a function of the normalized A_1 [Yu et al., 2019]. The slope will be the Strouhal number based on length (St_L) which is a constant value of about 0.23 for flags of flutter mode-2.

The limit cycle for the fluttering flag is also well documented in which clearly shows the instantaneous locations for a complete cycle [Eloy et al., 2008, Gibbs et al., 2014, Martin, 2006]. The flag will follow a continuous harmonic path with the free end having a path similar to the shape of the number "8", in which the flutter can be considered two-dimensional. Moreover, the shape of the flutter is shown through the use of imaging techniques. The surrounding fluid has been shown quantitatively for a straight state and a flutter state [Watanabe et al., 2002, Zhang et al., 2000]. For a straight state, the wake conditions will show the formation of Von-Karman vortex street. Upon flutter being induced, the Von-Karman vortex street will become large-scale vortices with small-scale Kelvin-Helm Instabilities. Due to the complex nature of the fluid flowing around a flag, advanced techniques, such as PIV, are needed to quantify the surrounding fluid field. The near-wall fluid has been analyzed for a mode-2 flutter that shows that flow does not separate [Gibbs et al., 2014]. Moreover, very little experimental work that analyzes the fluid wake and vortex shedding has been conducted.
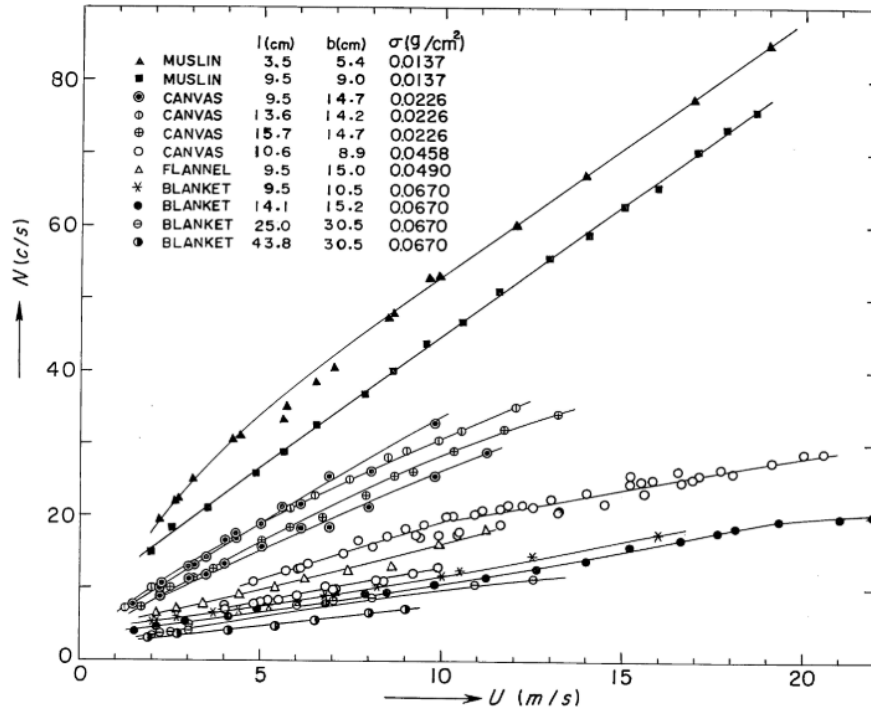
Figure 2.3: Fluid velocity as a function of dominant flutter frequency for various types of materials [Taneda, 1968].

As of the past few decades, interest in modeling interactions between flags and fluid has increased due to the improvement of computational power. Several methods have been created that model the flag and the fluid separately then couple them through a variety of techniques. The flag will be a variation of Equation 2.4 in either 1-D, 2-D, or 3-D. The fluid will either be considered potential flow [Argentina and Mahadevan, 2005, Alben and Shelley, 2008, Chen et al., 2014, Howell et al., 2009, Eloy et al., 2007, Michelin and Llewellyn Smith, 2009] or as the incompressible viscous N-S equation [Cisonni et al., 2017, Connell and Yue, 2007, Favier et al., 2014, Huang and Sung, 2010, Goza and Colonius, 2018]. Potential flow models tend to be easier to solve and give a good qualitative result but are limited by the non-local interactions and the three-dimensional effects that are limiting the accuracy of models [Argentina and Mahadevan, 2005]. In contrast, due to the high computational cost to model incompressible viscous N-S equations, it is still bottlenecked and only capable of modeling lower Re for values less than 1000. At this Re several phenomena previously mentioned are yet to occur. The fluid mode is then coupled to the structural model with either of the four possible techniques: theoretical linear stability [Argentina and Mahadevan, 2005, Goza and Colonius, 2018, Eloy et al., 2007], linear/nonlinear vortex lattice model [Alben and Shelley, 2008, Chen et al., 2014, Howell et al., 2009, Michelin and Llewellyn Smith, 2009], coupled fluid-structure direct simulation [Cisonni et al.,

2017, Connell and Yue, 2007], or immersed boundary method [Favier et al., 2014, Huang and Sung, 2010]. Each coupling technique differs based on model needed to comply with method of solving.

As previously stated, the flag problem captures the dynamics of flow over a cantilevered beam, which has several applications in engineering. Wings, tails, and panels in aircraft and spacecraft are also cantilevered structures submerged in a moving fluid. Though wing and tail orientation differ from the flag problem, understanding the flag problem, which is more complex due to the large displacement experienced, can aid in the understanding the aerodynamics of wings, tails, and panels. The flutter, due to FSI, of wings and tails has been known to cause catastrophic disintegration of the airplane while in flight [Goland, 1945, Loring, 1941]. In more recent times, a need more for efficient aircraft is driven by NASA's Green Aviation initiative [NASA, 2021], which aims to design an Ultra-Efficient Commercial Vehicle through various innovative means [Cavolowsky, 2017]. As a result, analysis has been conducted to study the flutter stability of high-aspect-ratio wings [Bottai et al., 2019]. This type of flutter is a self-sustained Limit Cycle Oscillation, in which a wing will remain in oscillatory motion, that will cause structural fatigue and failure. An extensive review on the topic has been covered on the numerical and experimental works in panel flutter [Dowell, 1970, Mei et al., 1999]. The FSI of panels is known to have a variety of modes at different velocities. Failure of panels has been seen due to the continuous stress from constant oscillation. In contrast, para-gliders, micro air vehicles [Haghighat et al., 2012, Ifju et al., 2002, Molki and Breuer, 2010, Rojratsirikul et al., 2010], parachutes [Peterson et al., 1996, Stein et al., 2000], and yacht sails [Augier et al., 2012, Trimarchi et al., 1970] take advantage of FSI to generate lift. The flexible structure, "flag wing," deformed by a fluid, will generate a reactive force [Molki and Breuer, 2010]. The flag wing will have the ends fixed with enough flexibility to deform to allow a concave deformation. This deformation will fill with ambient air to generate the force required to propel or lift the complete system, taking full advantage of FSI. These concepts stem from the idea of bio-mimicry, which takes advantage of nature's abilities to create and innovate current industrial applications.

In nature, several animals use the means of FSI to generate a propulsive force as a form of transportation. For example, fish are swimmers who use their entire body in an oscillatory motion to interact with the surrounding fluid to generate thrust and maneuver through bodies of water. The swimming fish has been reviewed, covering the analytic methods that have been done to measure and understand their propulsive mechanism [Sfakiotakis et al., 1999]. At the same time, birds and insects in other regards use the FSI phenomena to fly and navigate through the air. Biological flight has distinct differences from aircraft flight, which generally have fixed wings in large-scale applications. Biological fliers can glide by extending their wings or produce locomotion through the means of flapping their wings [Dhawan, 1991, Sane, 2003, Tobalske, 2007]. The flapping is a more complex motion in which a vortex

is generated in the wake to propel the biological flier. Bio-mimicry has inspired many to create micro air vehicles that fly utilizing flapping mechanism [Jiakun et al., 2020].

Two other industrial applications are energy harvesting and passive heat transfer. Application of energy harvesting extract energy from the fluid motion, which depends on the ability to keep a structure in constant oscillatory motion. Implementation is done with the use of the flag problem to extract the abundant energy from wind or water power through mechanical stresses [Giacomello and Porfiri, 2011, Li and Lipson, 2009, Orrego et al., 2017, Yu and Liu, 2016]. The use of piezoelectric material is common to substitute for the flag [Li and Lipson, 2009, Orrego et al., 2017, Yu and Liu, 2016], as well as the use of ionic polymer metal composites [Giacomello and Porfiri, 2011]. These smart materials convert mechanical vibration into electrical power. While in the case of heat transfer, the fluttering flag can be used to induce the transfer of heat [Gallegos and Sharma, 2017, Herrault et al., 2012, Lee et al., 2018]. Heat is transferred through the fluid mixing since the flutter of the flag is known to have a turbulent shedding in the wake region—turbulence in the fluid allowing for the passive transfer of heat in the fluid.

CHAPTER 3: EXPERIMENTAL SETUP

3.1 JET FACILITY

All the experiments for this study were conducted at the University of Idaho's Experimental Fluids and Aerodynamics Lab. An in-house free jet facility was used to provide uniform inflow for the standard flag problem. The jet system is shown in Figure 3.1. The fan inlet is located at the bottom right of the figure with a centrifugal fan, controlled with a DC motor, used to produce the flow. An Electro-Craft Corporation motor controller was used to control the RPM of the DC motor. The motor controller has a telescoping resistor dial, seen in Figure 3.2, which allows the jet to be varied from 0 to 1000 (RPM) with increments of 1 (RPM). The jet facility can produced flow from 0 m/s to 24 m/s with precise control at increments of 0.02 m/s. In the settling chamber, there are three sets of mesh and honeycomb layers for flow conditioning. A converging nozzle design was used for outlet flow with a diameter of $D_2 = 63.5mm$. Figure 3.3 shows the base plate that was used to hold the mounting mechanism apart from the jet system. Using a base plate would isolate the vibrations produced by the motor that could transfer during the load measurement experiments.
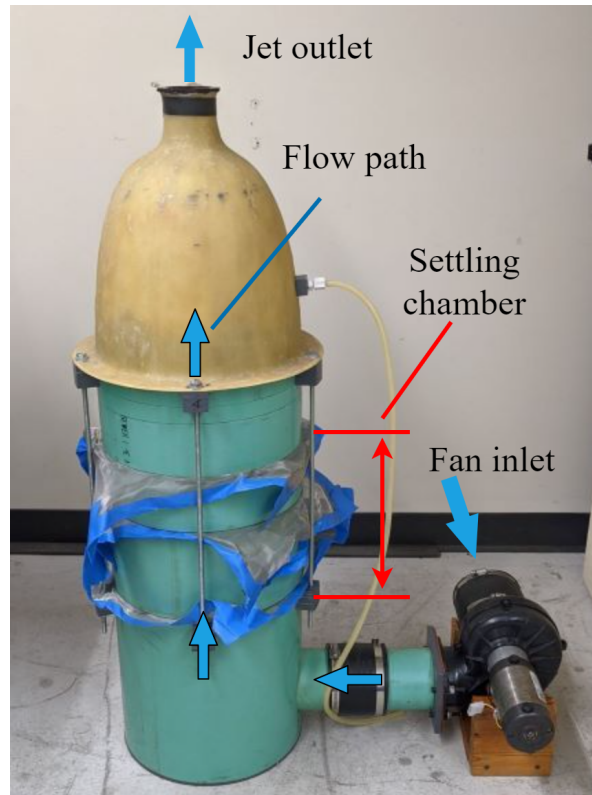
Figure 3.1: Free jet used to provide the fluid source.
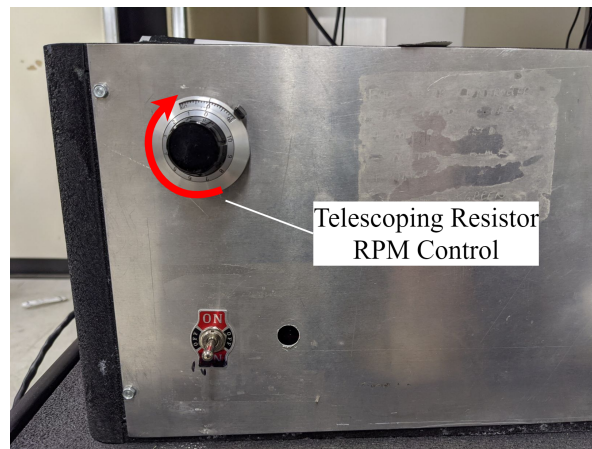
Figure 3.2: Electro-Craft Corporation motor controller with telescoping resistor for setting RPM.

Figure 3.3: Free jet system with the surrounding base plate that will isolate the samples.

3.2 MOUNTING MECHANISM

The mounting mechanism and a sample of interest are as shown in Figure 3.4 along with the coordinate system at the flags fixed leading edge. Based on position of the jet, y(+) is in the direction of the flow. A clamping mechanism was used to fix the flag at the leading edge, with a close-up shown in Figure 3.5. Tension is applied in the direction shown to ensure that the flag's leading-edge remains properly fixed and taut. This stand allows to properly position the flag at the center of the jet outlet and setting a proper angle of attack using the rotating mechanism shown in Figure 3.4. To ensure the mounting stand was not affected by the fluid flow, a diameter D_1 was designed to be two times larger than the outlet jet diameter D_2. The mounting stand is only attached to the marked loadcell location, which is also shown in Figure 3.4. A direct attachment ensures the loadcell measures all forces experienced by the flag and allows for the loadcell to measure lift and drag in the x-direction and y-direction, respectively. Alignment is checked before every experiment is conducted by ensuring an average of zero lift was generated.
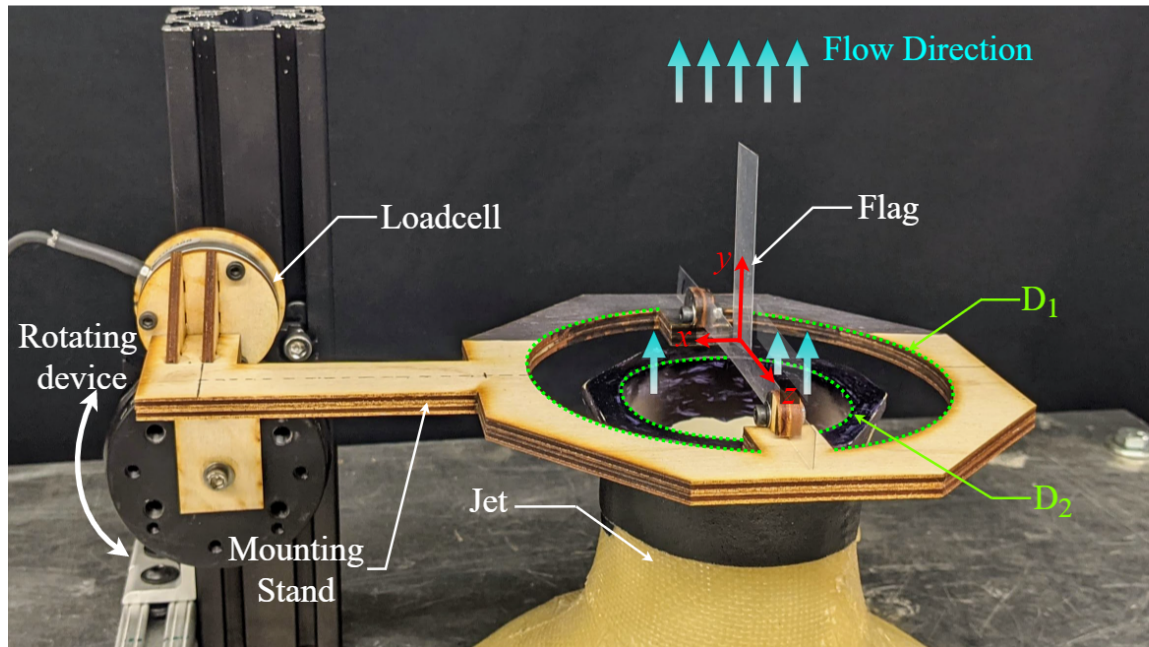
Figure 3.4: The experimental set-up used for the presented studies. The flow direction is indicated along the y-axis with the flag placed at the outlet of the jet. The flag stand is directly attached to the loadcell.
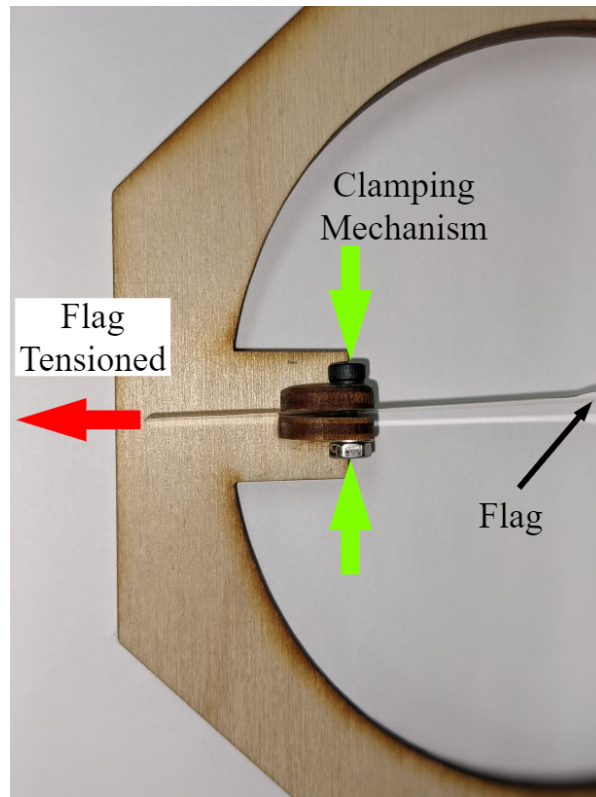
Figure 3.5: Clamping mechanism to secure the flag samples and fix the leading edge.

3.3 JET VELOCITY CALIBRATION

A free jet fluid source allowed us to avoid the issue of blockage during flag fluttering [Tang et al., 2007]. Before the experiments, the jet was calibrated using the jet exit velocity U_∞ as a function of motor controlled RPM. The U_∞ was measured using PIV measurements as a reference. Moreover, 1000 PIV images were used for each selected U_∞ at an RPM value. Figure 3.6 shows the 5 calibration points and curve fit, resulting in a calibrated U_∞ as a function of RPM as,

$$U_\infty = 0.024(RPM) - 0.430. \tag{3.1}$$
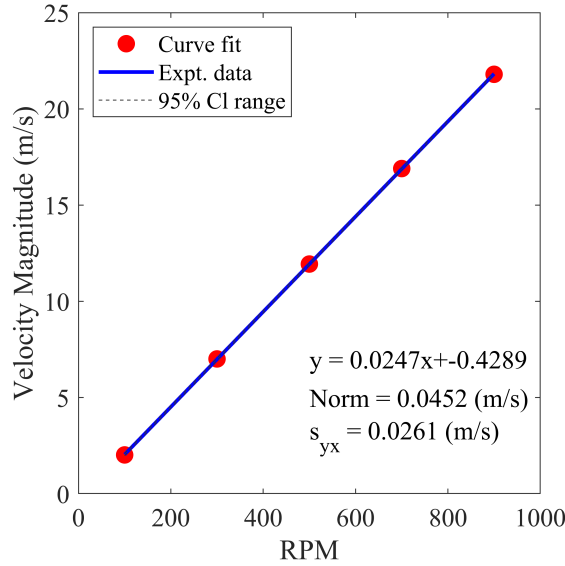
Figure 3.6: Calibration of the jet facility outlet velocity based on RPM controller. Shown with curve fit and a 95% certainty.

3.4 FLAG SAMPLES

For this study, three different flag samples were used as shown in Figure 3.7. The flag samples were created to be easily attached to the mounting mechanism and were clamped in the "Clamped region". The samples selected were cut from a cellulose acetate material seen in Figure 3.4. Sheets of cellulose acetate material were used, so minimum possible planiety defects were seen, which can lead to a change in dynamics of the flutter [Eloy et al., 2012]. Dimensions could be seen in Figure 3.8 with the thickness h being around 0.1 m, width w being around 0.02 (mm), and of varying lengths L. The leading edge is the edge where inlet velocity is provided, and the trailing edge is the free end with its

path indicated in Figure 3.8. Three samples were created of lengths: 0.041 m, 0.053 m, and 0.07938 m, with the names that will be used for the, remained for the paper, Sample #1, Sample #2, and Sample #3, respectively. The complete list of geometry properties for the associated sample can be seen in Table 3.1. The Young's modulus for the material was 3.89 ± 0.37 GPa measured with a Model 5944 Materials Testing System, with complete details on measurements discussed in chapter 4. Measured values are within range of provided value by the manufacture. The h and flag width (mm) (w) for the samples were kept constant only to vary the mass ratio based on the sample L.
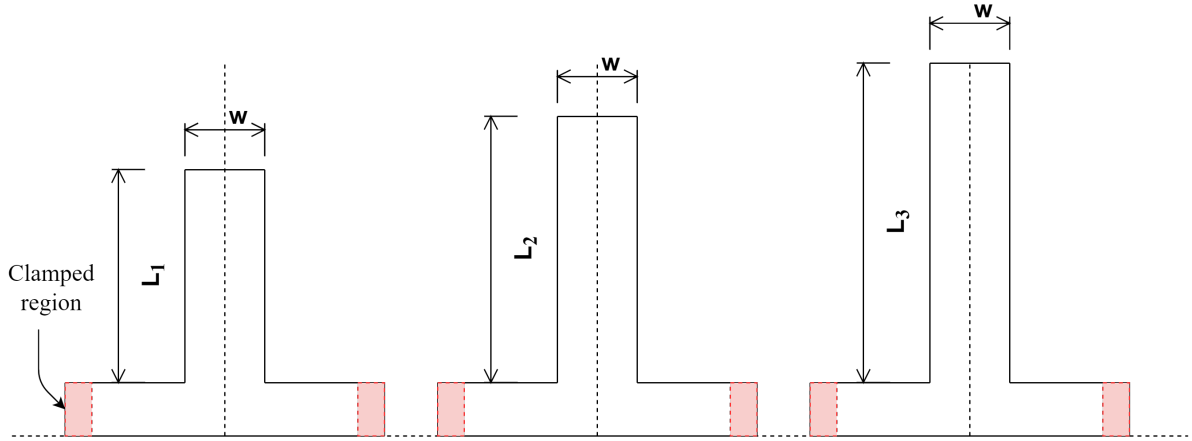
Figure 3.7: Schematic of the three samples used with the distinguishable lengths of: sample 1) $L_1 = 41.67$ mm, sample 2) $L_2 = 53.96$ mm, and sample 3) $L_3 = 79.38$ mm.

Table 3.1: Geometry of the three samples that are being investigated in the study.

Sample	Thickness(mm)	Width(mm)	Length(mm)
#1	0.098 ± 0.0047	20.0 ± 0.31	41.67 ± 0.22
#2	0.097 ± 0.0047	20.1 ± 0.19	53.96 ± 0.32
#3	0.099 ± 0.0083	20.1 ± 0.42	79.38 ± 0.13

3.5 FORCE AND TORQUE TRANSDUCER

An ATI Mini 40 SI-20-1 force and torque transducer was used to measure the aerodynamic loads experienced by the flag. The transducer that is attached to the stand is shown in Figure 3.9. The aerodynamic loads of the flag flutter are lift and drag with the relationship with the x-direction and y-direction, respectively. Aerodynamic values are measurable up to 20N with a resolution of 0.005N and transverse load measuring up to 60N, and a resolution of 0.01N. An NI data acquisition was used to sample at a rate of 500 Hz for 60 seconds. This procedure was done for each incremental change in velocity until reaching the maximum velocity that resulted in time-series data. This was
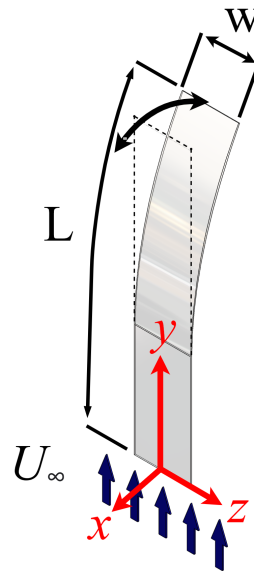
Figure 3.8: Isometric View of a flag deflected for a mode-2 flutter type. The flow direction is indicated along the y-axis as to be parallel with the flag and in the direction of drag. Lift will be measured along the x-axis and fluttering direction.

done to achieve a single time-averaged lift and drag data result at the varying velocities. Studies were repeated three independent times to ensure the accuracy of the results. Before each run, the local atmospheric pressure and temperature was measured with a digital barometer and digital thermometer, respectively. In addition, initial iterative measurements were conducted to verify that zero lift on average was experienced during the flags straight state and flutter state.
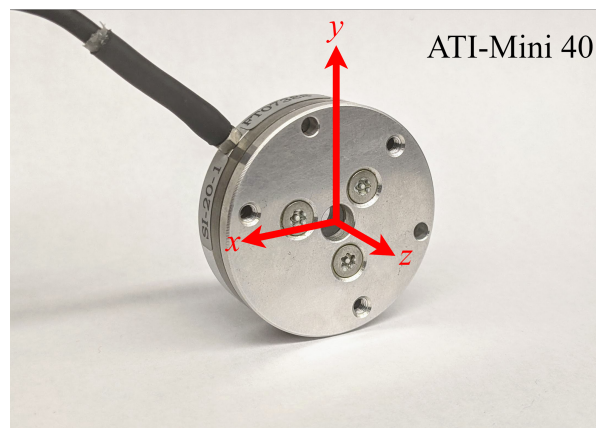
Figure 3.9: ATI-Mini 40 force and torque transducer with the indicated axis relative to the flag in Figure 3.8.

3.6 Particle Image Velocimetry

It was desired to observe and quantify the fluid field surrounding the flag flutter and spatially define the flag to a corresponding velocity field. For this purpose, a particle image velocimetry (PIV) system was used to conduct these experiments [Raffel et al., 2018]. A PIV is an optic based method to visualize flow fields. The PIV used is a LaVision Evergreen Nd:YAG 200 mJ dual pulsed laser capable of pulsing at 15 Hz. Triggered along with the PIV was a 6 MP Imager SX dual-frame CCD camera with a lens attachment of 50 mm to be triggered at 13 Hz. Moreover, a programmable timing units by LaVision is employed to synchronize the triggering of the laser and camera. The two-dimensional plane produced by the laser sheet is shown, Figure 3.10, as a green light sheet. This laser sheet is triggered by the "Q-Switch Tigger 1" for "Laser Emission 1" and "Q-Switch Tigger 2" for "Laser Emission 2" in Figure 3.11. The laser is produced initially as a thin laser point that is then fanned out through optical lenses to make the laser sheet. Due to the nature of this, the laser must be appropriately configured to have the thinnest part of the sheet converge at the location of interest, which is the location of the flag in Figure 3.10. Consideration to make sure the field of view is correct must also be done. Proper placement ensures the fanned-out laser sheet covers the field of view shown in 3.10. This field of view needs to be perpendicular to the camera being used for imaging.

Once proper positioning is achieved, proper triggering times must be selected. With the current setup of the two-dimensional flow, the fluid particles illuminated are the seeding particle (Di-Ethyl-Hexyl-Sebcat; DEHS) that a LaVision Aerosol Generator anodized. This seeding particle was feed at the fan inlet to come out laminar from the jet outlet. The particle displacement based on the inlet velocity will aid in the proper selection of the triggering times. As seen in figure 3.11 the "Emission" times will fall with two times of the "Camera Double Exposure" that are related to Image #1 and Image #2. The camera triggering was set to be before the "Emission" to ensure the proper imaging of the illuminated particles. Proper exposure time should be set to make the particles as clear as possible. If particle streaking occurs, proper processing will not be achievable. Once proper exposure time is selected, a time difference between "Laser Emissions 1" and "Laser Emissions 2" must be selected. This time difference is dt in Figure 3.11. The dt will depend on the intended interrogation window of interest based on a $pixel \times pixel$ window size. From this, a particle should travel 1/8 of the interrogation window to extract a vector from this window. An interactive process is done at the beginning of each PIV study to select proper values and ensure the best quality of data is collected.

The results of this process would be two images of the known time difference, dt. These two images are then divided into $N \times N$ interrogation windows of $pixel \times pixel$ size as shown in Figure 3.12. Separate
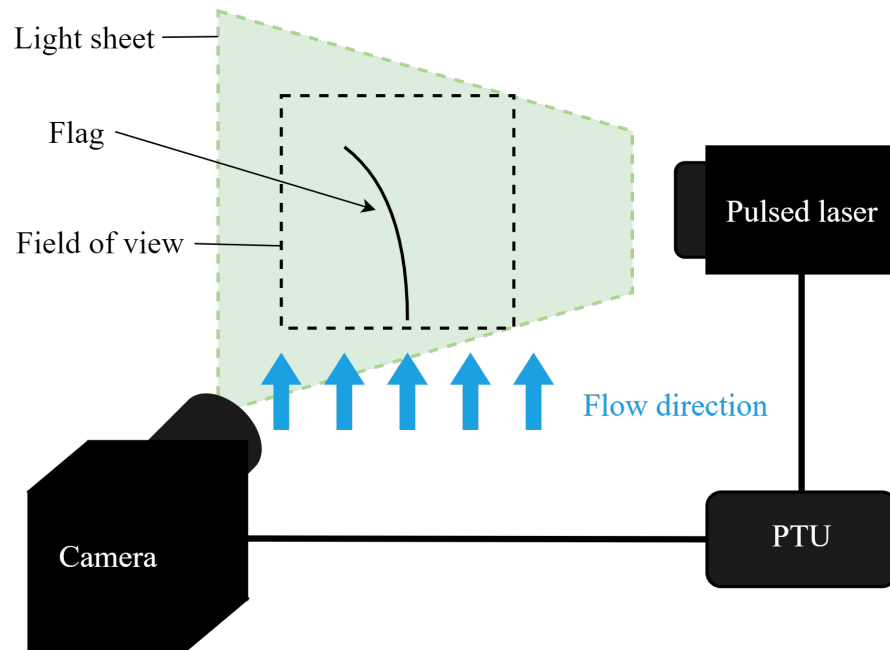
Figure 3.10: The configuration for the Particle Image Velocimetry. The light sheet is created by the pulsed laser. The field of view is observing the flag and a wake region which is captured by the camera. The pulsed laser and camera are triggered based on the timing diagram by the programmable timing unit.

interrogation windows can then be investigated with similar positions in the images. Processing is done in the proprietary software by LaVision, DaVis, through a cross-correlation in which the individual particles can be traced to find an averaged displacement per interrogation windows. This displacement is divided by the known time difference, dt, to give a local velocity. Cross-correlation is done to the complete image that results in a vector velocity field for fluid displacement at a given time. For the current study 1000 images are taken for each PIV study resulting in 1000 vector velocity fields per Reynolds number as seen in Tables A.1 - A.3.
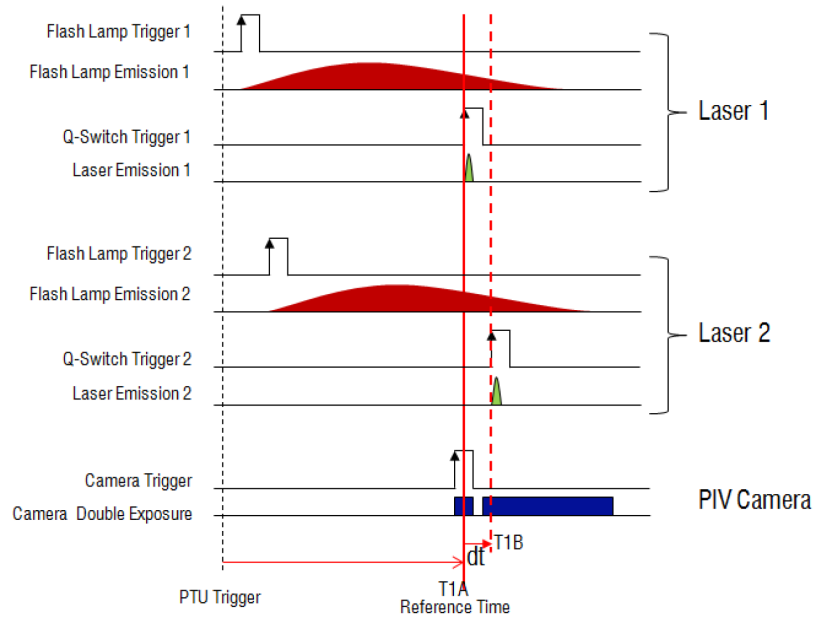
Figure 3.11: The timing diagram for the pulsing of laser #1 and #2 along with the triggering of the camera.
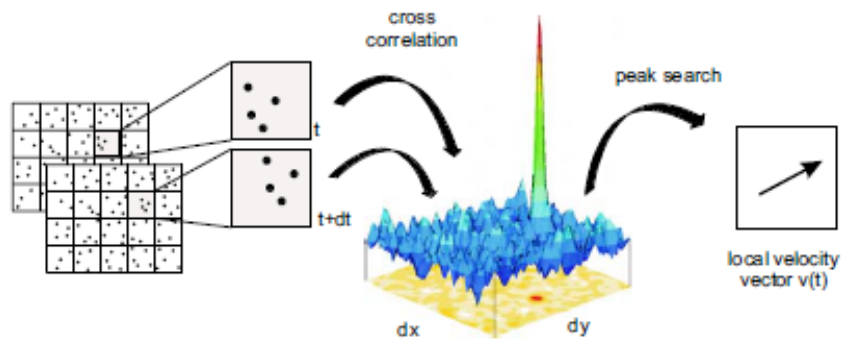
Figure 3.12: The two produced PIV images broken into interrogation windows for cross correlation.

CHAPTER 4: UNCERTAINTY ANALYSIS

For this study, the uncertainty of the drag coefficient, C_D, and Young's modulus, E, are estimated. For the C_D uncertainty propagation of error is utilized as shown in equation 4. With equation 4 being for the C_D.

$$u_R = \sqrt{\sum_{i=1}^{M} (\omega_i u_{\bar{x}_i})^2} \quad ; \quad \omega_i = \frac{\partial R}{\partial x_{i_{x=\bar{x}}}} \quad ; \quad i = 1, 2, ..., M \tag{4.1}$$

$$C_D = \frac{F_d}{\frac{1}{2}\rho_f U_\infty^2 A} \tag{4.2}$$

Propagation of error was then applied the drag coefficient for the provided equation 4. In this equation, the uncertainty of the drag force, inlet velocity, and the characteristic area are considered. Furthermore, multiple measurements of each term were performed to ensure accuracy, and a sample of size, N, was collected for the length, width, thickness, and forces. The sample mean and related uncertainty is based on equations 4.4-4.6 are substituted into equation 4.3:

$$u_{C_D} = \sqrt{\left(\frac{\partial C_D}{\partial F_D}u_{F_D}\right)^2 + \left(\frac{\partial C_D}{\partial \rho_f}u_{\rho_f}\right)^2 + \left(\frac{\partial C_D}{\partial U_\infty}u_{U_\infty}\right)^2 + \left(\frac{\partial C_D}{\partial A}u_A\right)^2}, \tag{4.3}$$

$$u_{F_D} = \frac{t_{\nu_{D,P}}s_F}{\sqrt{N}}, \tag{4.4}$$

$$u_{U_\infty} = \frac{t_{\nu_{D,P}}s_{xy}}{\sqrt{N}}, and \tag{4.5}$$

$$u_A = \frac{t_{\nu_{D,P}}s_A}{\sqrt{N}}. \tag{4.6}$$

$$\tag{4.7}$$

The measurements used for the characteristic area were length and width of the flag was measured using a dial caliper with a resolution of $2.54 \times 10^{-5}(m)$. The thickness was measured with a micrometer with a resolution of $2.54 \times 10^{-6}(m)$. Sampling was taken at several random locations. Based on a 95% certainty, the results in uncertainties values are 0.9% for length measurements, 0.6% for width measurements, and 0.01% for thickness. As for force measurements, sampling was done for 60 seconds at a rate 0f 500 Hz to acquired the time-averaged drag force. Due to the nature of the flag problem, two

possible states, non-oscillatory and oscillatory state, with two different uncertainty behavior. Moreover, non-oscillatory measurements are small and close to the load-cell's resolution and will not be considered. For oscillatory measurements the maximum uncertainties at higher Re for sample #1, #2, and #3 will be 0.89%, 3.08%, and 2.018%, respectively.

These measured values and uncertainty can then be applied to equation 4 to find the 95 % uncertainty in Drag Coefficient. For the Drag Coefficient, the most significant contributor to the uncertainty was the force measurement which depends on the state of the membrane. Resulting in a maximum uncertainty for drag coefficient in an oscillatory state is a maximum value of 3.29 %. This translates to considerably low uncertainty values for the fluttering state, which agrees with the repeated studies.

The young's modulus was acquired from the provided spec sheet for the material and verified through tensile testing of five samples. In addition, the ASTM D882 standard was followed with measurements read from a Static 2kN range load cell. These five samples were measured from zero loading until a yield point was reached. The resulting stress-strain plot is shown in Figure 4.1, along with the linear region to acquire Young's modulus. The slope of the linear region is $0.3739GPa/(mm/mm)$ with a y-intercept of 0.063 GPa and uncertainty of $\pm0.13GPa$. Thus, compared to manufacturers spec, the results are within 2.7% of the provided Young's modulus.
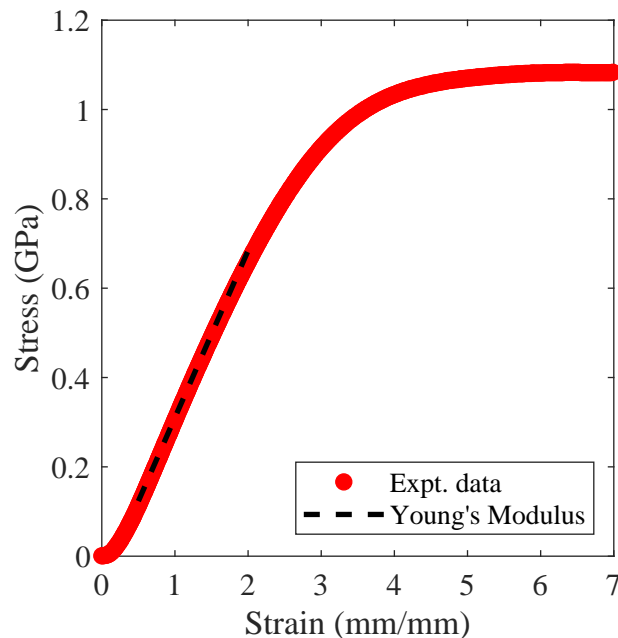
Figure 4.1: Stress versus strain plot for the cellulose acetate material to measure the Young's modulus.

Chapter 5: Test Matrix

Three sample were used for this study and that will be referenced with the following notation sample #1, #2, and #3. The key non-dimensional parameters selected for this study are the mass ratio R_1, dimensionless rigidity R_2, and Reynolds number Re. The analysis of the samples included aerodynamic loads, membrane location of coherent flutter mode, and PIV analysis for averaged velocity field during flutter. Table 5.1, shows the range of values for the mentioned key terms and experiments conducted. The complete set of data for Re increments of each are listed in Appendix A tables A.1-A.3.

Table 5.1: Table of associated non-dimensional values and studies for the three samples of the investigation with symbols $\bullet, \diamond$, and $\star$ for load measurements, imaging, and PIV, respectively.

Sample	$Re(10^3)$	R_1	$R_2(10^{-3})$	AR	Measurement
#1	56 - 75	2.77	8.0 - 14.5	0.48	$\bullet, \diamond, \star$
#2	53 - 84	2.14	4.1 - 10.3	0.37	$\bullet, \diamond, \star$
#3	44 - 123	1.48	1.3 - 10.1	0.25	$\bullet, \diamond, \star$

CHAPTER 6: RESULTS

The following section includes the discussion of the obtained experimental measurements that were acquired through the conducted study. Discussion will begin with the introduction of the aerodynamic performance of the flag. Followed by the defined characteristics of the fluttering flag for the averaged coherent flutter behavior. Lastly, the averaged velocity field will be discussed for selected cases.

6.1 AERODYNAMICS

Drag and lift forces were measured using the ATI-Mini force and torque transducer for a range of Re. These values were was used to calculate the C_L and drag coefficient (C_D). The time series sample data for the C_L and the C_D at the Re of 90×10^3 is presented in Figure 6.1(i) and 6.1(ii), respectively, showing the initial 0.5 seconds. This figure shows the fluctuations experienced during the flutter cycle for both lift and drag. Lift coefficient is centered about the a value for a mean $C_L = 0$, as shown in Figure 6.1(i). While for this case, the drag coefficient is centered around the value of 0.17, as shown in Figure 6.1(ii).
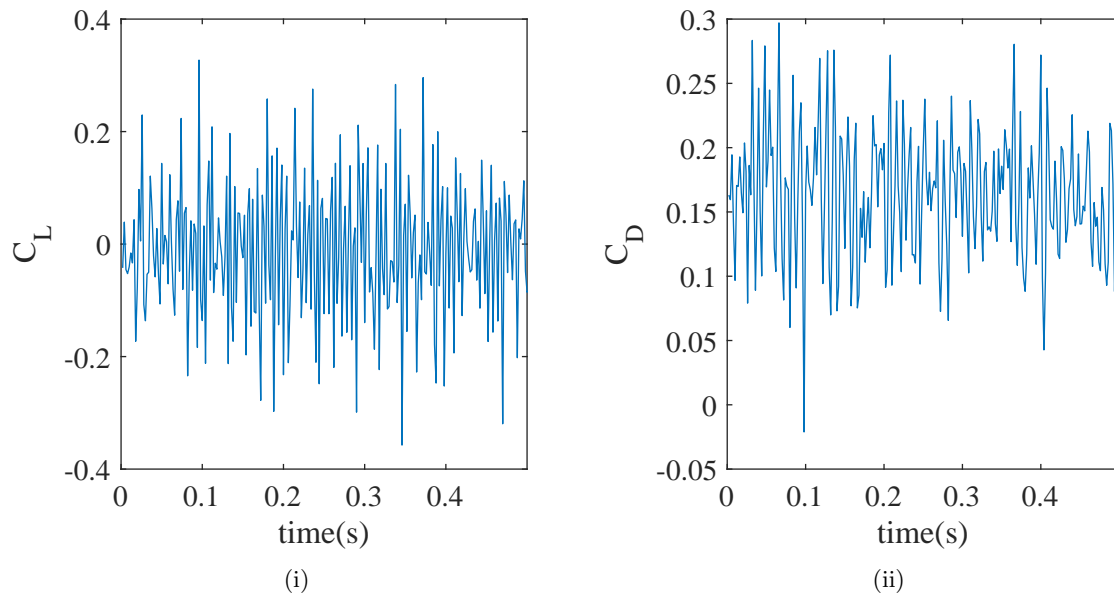
Figure 6.1: Respective data set for half a second sample time for the drag coefficient (i) and lift coefficient (ii) at a Re of 90×10^3.

The time-averaged C_D value is extracted from the time-series and plotted as a function of Re for sample #1, #2, and #3 in Figures 6.2(i), 6.2(ii), and 6.2(iii), respectively. On these figures, the theoretical C_D scenario for drag experienced on two sides of a plate is plotted as a black dotted line

(i) Sample #1

(ii) Sample #2

(iii) Sample #3
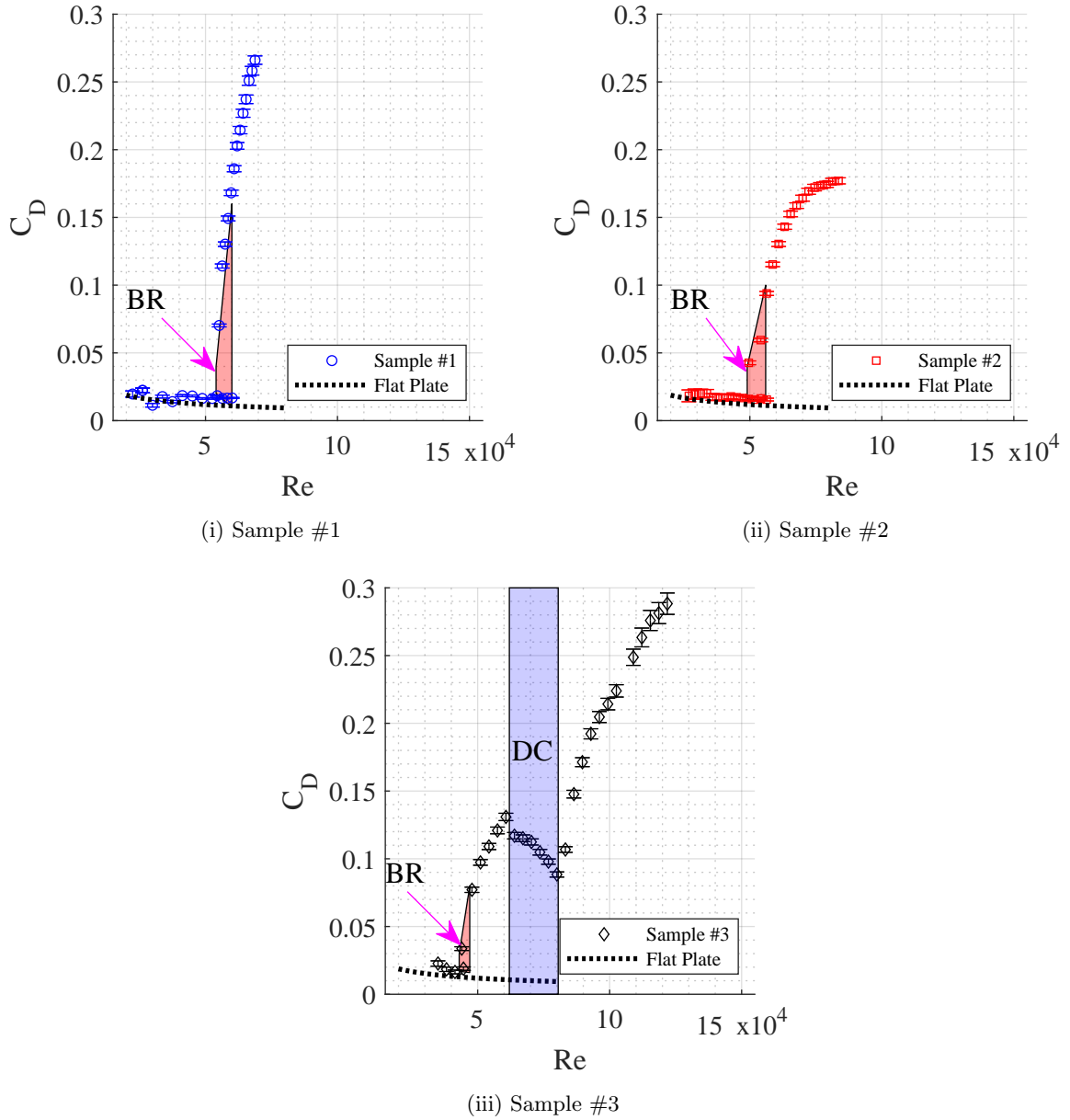
Figure 6.2: The drag coefficient (C_D) as a function of Reynolds number (Re) for samples #1 - 3. Bifurcation region (BR) is shown as the red shaded region.

that is calculated using Blasius solution for flat-plate flow [White, 2006]. The non-oscillatory region Re values are from 22×10^3 to 60×10^3, 27×10^3 to 57×10^3, and 32×10^3 to 45×10^3 for sample #1, sample #2, and sample #3, respectively. This region indicates that when the flag is in a straight state, the flag will experience a decrease in the C_D with the increasing Re closely matching the solution for the C_D of two side of a flat-plate. Uncertainty bars have been added to their corresponding time-averaged

C_D value with uncertainty bars that are within the marker size. The U_d for sample #1, #2, and #3 is 17.25m/s (Re = 54×10^3), 13.07m/s ($Re = 50 \times 10^3$), and 8.17m/s (Re = 44×10^3), respectively, which is in agreement with Huang [Huang, 1995]. It was shown experimentally that with an increasing length, the critical velocity would decrease. The higher critical velocity value is the U_d, with higher velocities always being oscillatory. The corresponding values for sample #1, #2, and #3 being 19.04m/s (Re = 60×10^3), 14.86m/s ($Re = 57 \times 10^3$), and 8.29m/s (Re = 45k), respectively. Figure 6.2 shows the hysteresis loop which is the range of velocities bounded by U_d and U_c values, known as the bifurcation region (BR). These are shown in the figures as the red-shaded region. Within these bounds the flag can be in either an oscillatory or non-oscillatory state. For the samples presented, sample #1 will have the largest hysteresis loop, and sample #3 will have the smallest.
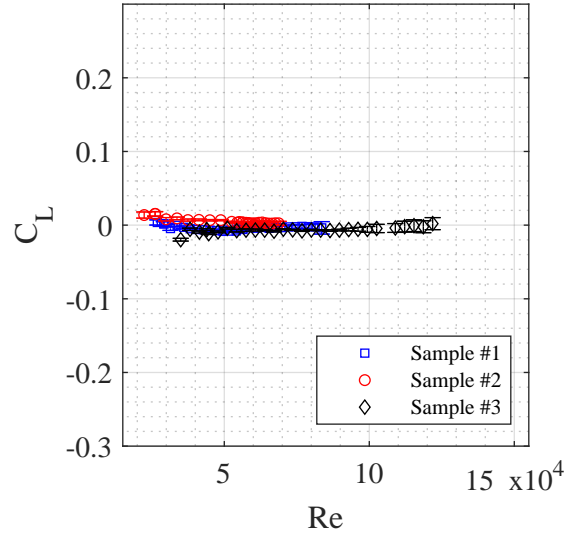
Figure 6.3: The lift coefficient (C_L) as a function of Reynolds number (Re) for samples #1 - 3.

Post U_c, three distinct regions are defined. The first region is the normal flag drag behavior which is observed in all three samples. Occurring once the flag initially becomes unstable, a sudden increase in drag is experienced by the flag with the increasing Re [Virot et al., 2013]. The ranges of the Re will be 54k to 75k for sample #1, 50k to 84k for sample #2, and 44k to 123k for sample #3. Followed by two regions that will only apply to sample #3. The primary region is known as the drag crisis (DC), which is similar to observations made by Carruther and Fillipone [Carruthers and Filippone, 2005]. The drag crisis begins at the local maximum C_D of 0.13, the C_D will begin to decrease with the increasing Re. This is highlighted by the blue rectangular zone, for the Re of 61k to 81k that will reach a local minimum C_D of 0.089. The final region will follow the drag crisis, which is called the drag recovery

region. The drag will be increasing as the Re increases and with Re of $81k$ to $123k$. The flag behavior will be further explored in the following sections.

Time-averaged values were also done for the C_L. The values for sample #1, #2, and #3 for all the Re are shown in Figure 6.3. Further investigation shows that all time-averaged C_L values are around zero. A value of zero is indicative of symmetric flutter behavior based on lift generation regardless of flutter behavior presented.

The C_D as a function of R_2 is shown on Figure 6.4 (i), 6.4 (ii), and 6.4 (iii) for sample #1, for sample #2, and for sample #3, respectively. These figures show distinct differences between the three samples and that higher values of R_2, which are at lower velocities, will have lower C_D. As the velocities increase R_2 will decrease, or becoming less rigid, and C_D will increase. With sample #1 the flag rapidly becomes less stiff with the increasing C_D. The sample #2 has two distinct regions which are the drag increases at a higher rate from R_2 7.2 to $10.3(\times 10^{-3})$ and for R_2 4.1 to $7.2(\times 10^{-3})$ the C_D will begin to 0.19. As for sample #3, it will contain the three prior regions. The initial normal flag drag behavior is linear for the region of R_2 5.3 to $10.1(\times 10^{-3})$. Following is the drag crisis region will have a R_2 region from 3.3 to $5.3(\times 10^{-3})$ and the final drag recover region for R_2 will be from 2.0 to $3.3(\times 10^{-3})$.

(i) Sample #1

(ii) Sample #2

(iii) Sample #3
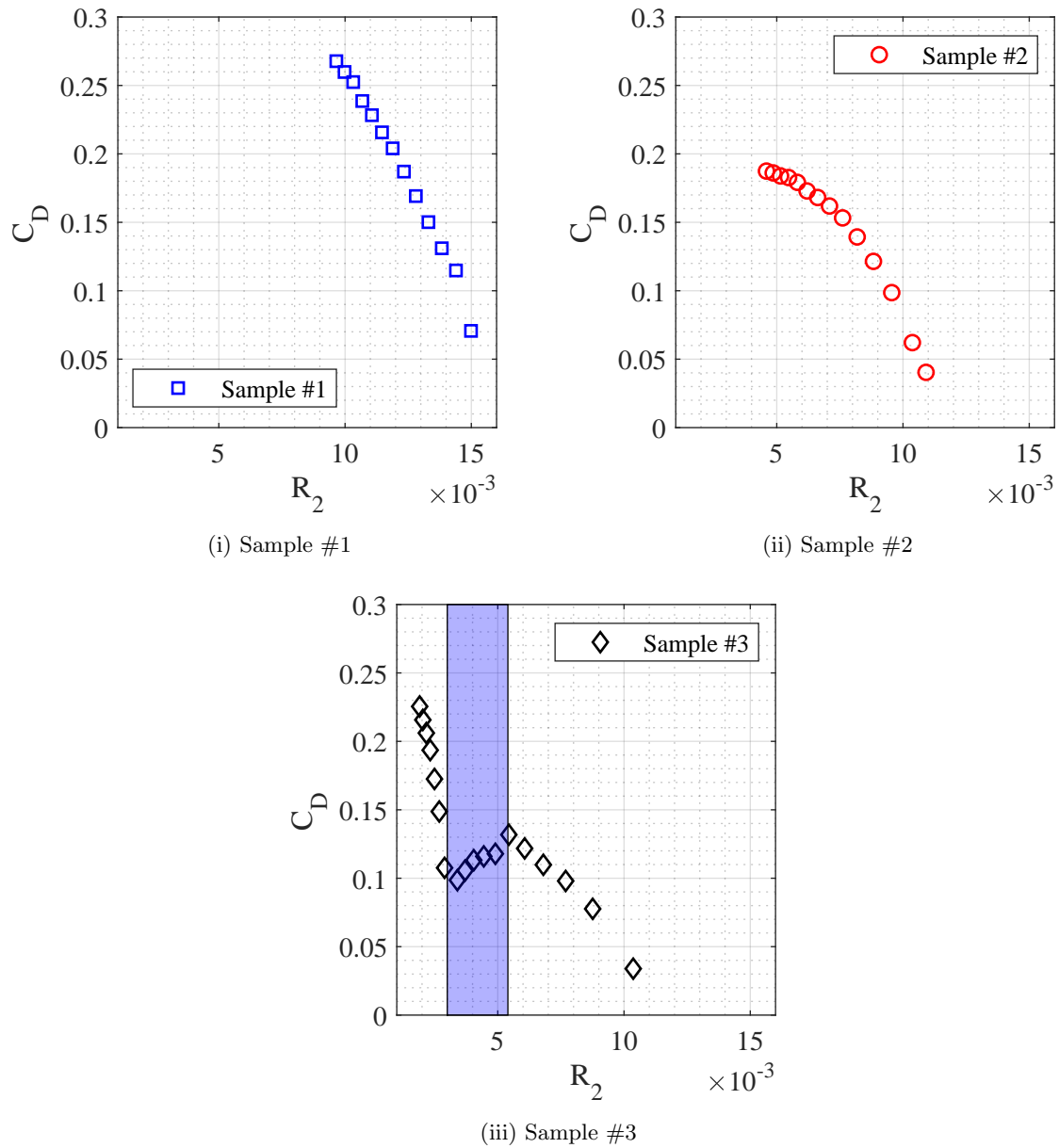
Figure 6.4: The drag coefficient C_D as a function of Reynolds number Re for samples #1 - 3: indicating the bifurcation region (BR) drag crisis region (DC).

6.2 Flag Shape

The averaged coherent flag shape is acquired from the overlaid images of the complete flutter cycle. All coherent shapes for the samples are shown in Figure 6.5, 6.6, and 6.7 for sample #1, #2, and #3, respectively. From these figures, distinct shapes can be identified. Figure 6.5 shows the development of all the sample #1 flutter cases in a mode-2. In figure 6.6, the straight state of the flag for sample #2 is shown in image (A). Following with the mode-2 coherent flutter shape, which is images (B)-(O) in figure 6.6. As for sample #3 images (A)-(K) in figure 6.7 will be experiencing mode-3 flutter behavior. Mode shapes change and with a A_2 is observed for sample #3 seen in Image (L) and images (M)-(S) in 6.7, respectively.
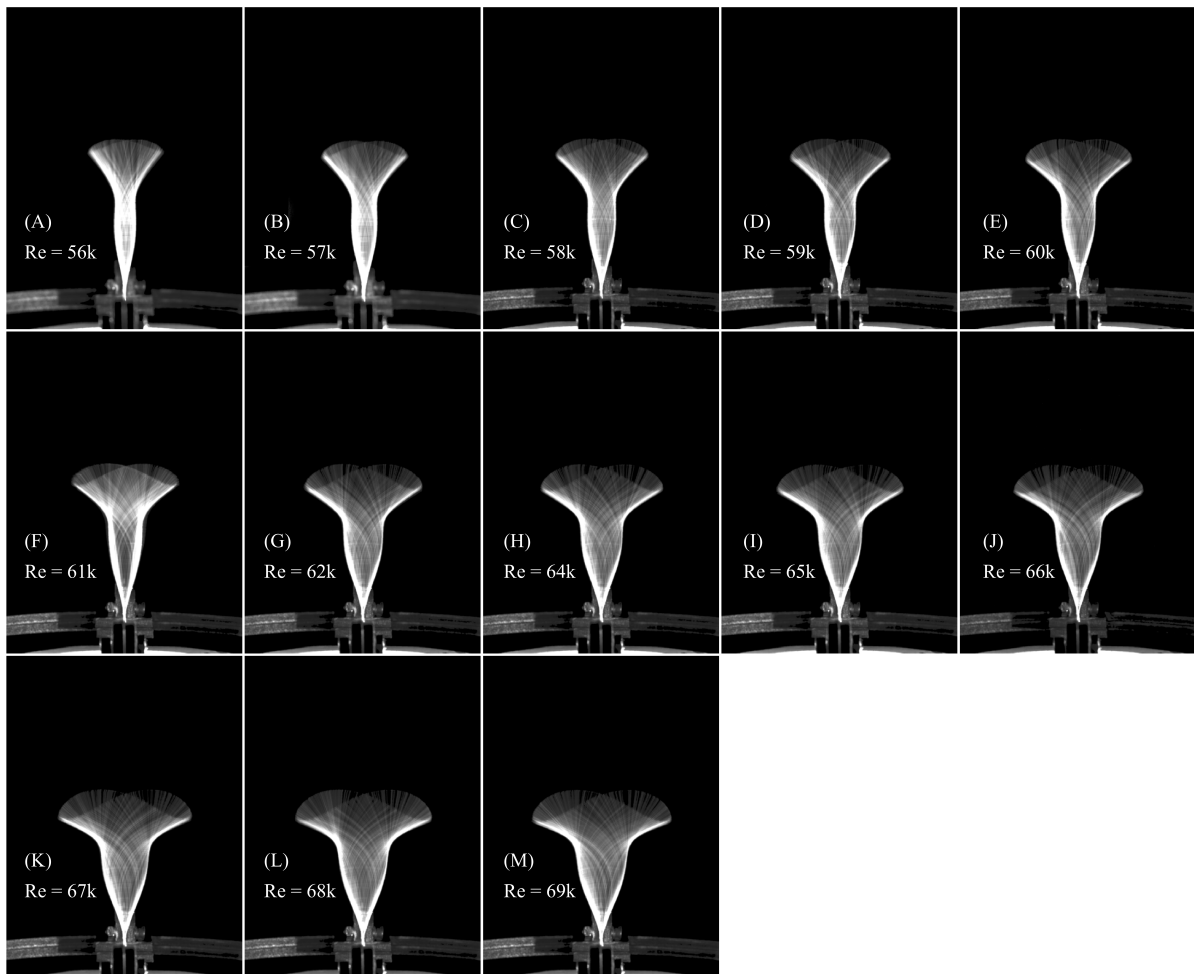
Figure 6.5: Flutter mode development for sample #1 flag flutter with increasing Re.
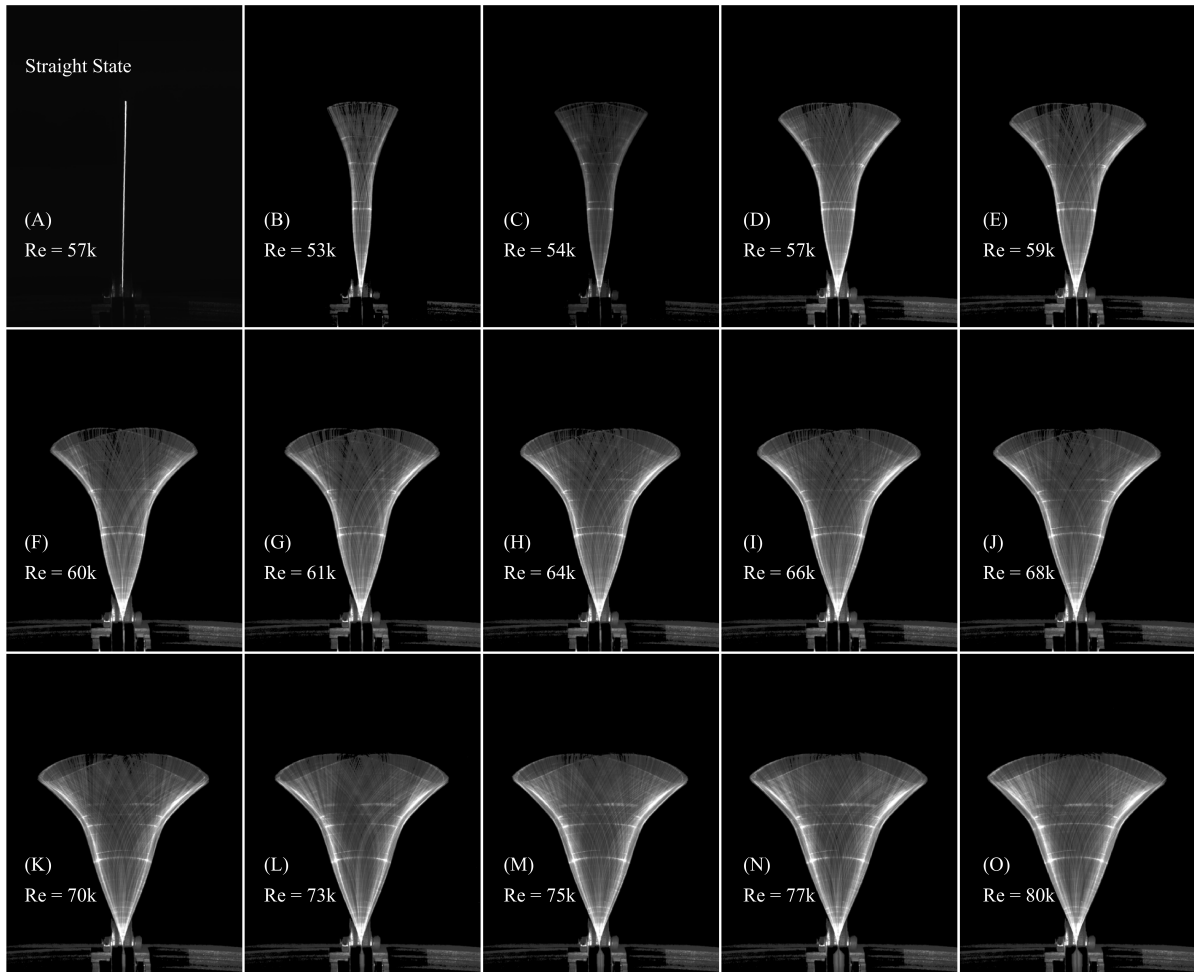
Figure 6.6: Flutter mode development for sample #2 flag flutter with increasing Re.
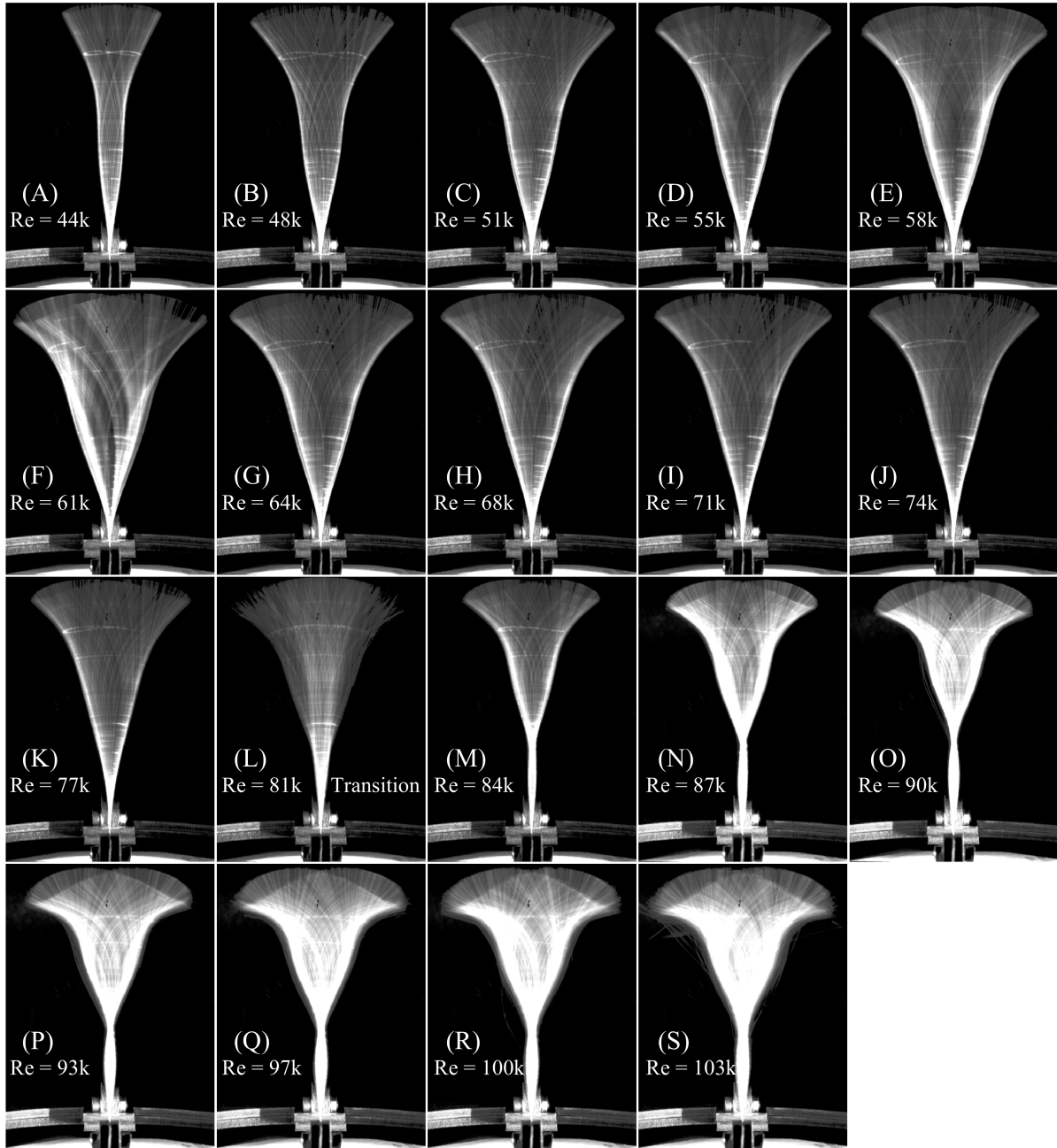
Figure 6.7: Flutter mode development for sample #3 flag flutter with increasing Re.

Figure 6.8 and 6.9 will be used to define the characteristics of the flutter behavior for mode-2 and mode-3. Various polynomial functions can be used to define the envelopes of flutter. These are shown as the red line in figure 6.8 and 6.9. From this defined functions the amplitude of oscillation A_1, second amplitude of oscillation A_2 and amplitude of neck N_e can be defined mathematically and will be defined based on x-axes displacements. Shown on the figure 6.8 and 6.9, A_1, N_e, and A_2 will be the minimums & maximums, inflection points, and local minimums & maximums of the lens shaped region near y = 0, respectively. These are indicated by the green arrows in the figures. The left and right most position will define the A_1. The N_e is the the region where the amplitude is locally small that is quantified by taking the second derivative of the polynomial function. Furthermore, the A_2 is calculated by taking the first derivative of the polynomial function, respectively. All result values have been tabulated in the appendix on table A.1, table A.2, and table A.3 for sample #1, #2, and #3, respectively.
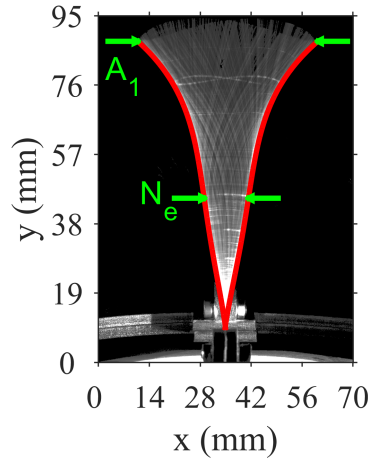
Figure 6.8: The averaged flag flutter for sample #3 at a Re of 48k. This is case (**A**) with the amplitude of oscillation denoted as A_1 and the neck as N_e.
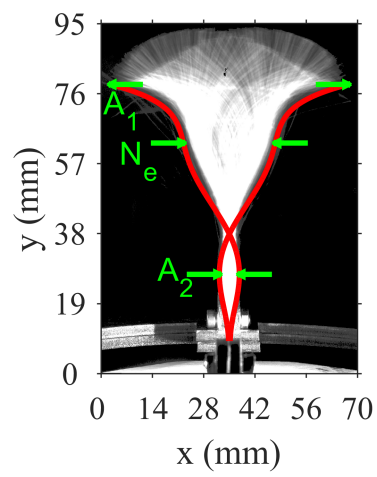
Figure 6.9: The averaged flag flutter for sample #3 at a Re of 103k. This is case (**B**) with the amplitude of oscillation denoted as A_1, the neck as N_e, and the second amplitude of oscillation A_2.

6.2.1 Flag Characteristics

The ratio of the amplitude of oscillation normalized by flag length (A_L) is,

$$A_L = \frac{A_1}{L} \tag{6.1}$$

and is plotted as a function of Re are plotted in Figure 6.10 (i)-(iii) for samples #1, #2, and #3, respectively. For sample #1 amplitude growth is large with the increasing Re and grows to a maximum A_L of 1. As for sample #2 the amplitude growth is large for Re from $57k$ to $73k$ this is followed by a decrease in amplitude growth rate from $73k$ to $84k$. Sample #2 will also have a maximum A_L ratio of 1. Sample #3 on the other hand experiences three changes in amplitude of oscillation development. For the Re range from $44k$ to $61k$ the amplitude will be increasing. This will reach a maximum A_L ratio of 0.8. Following is the decrease in amplitude of oscillation for the Re from $61k$ to $81k$. This will reach a minimum A_1 to L ratio of 0.57. A mode change from mode-2 to mode-3 is also experienced at the Re of $81k$ for sample #3, which leads to the final change in the amplitude of oscillation that will be increasing from $81k$ to $103k$. This will reach a maximum A_L ratio of 0.83.

(i) Sample #1

(ii) Sample #2

(iii) Sample #3
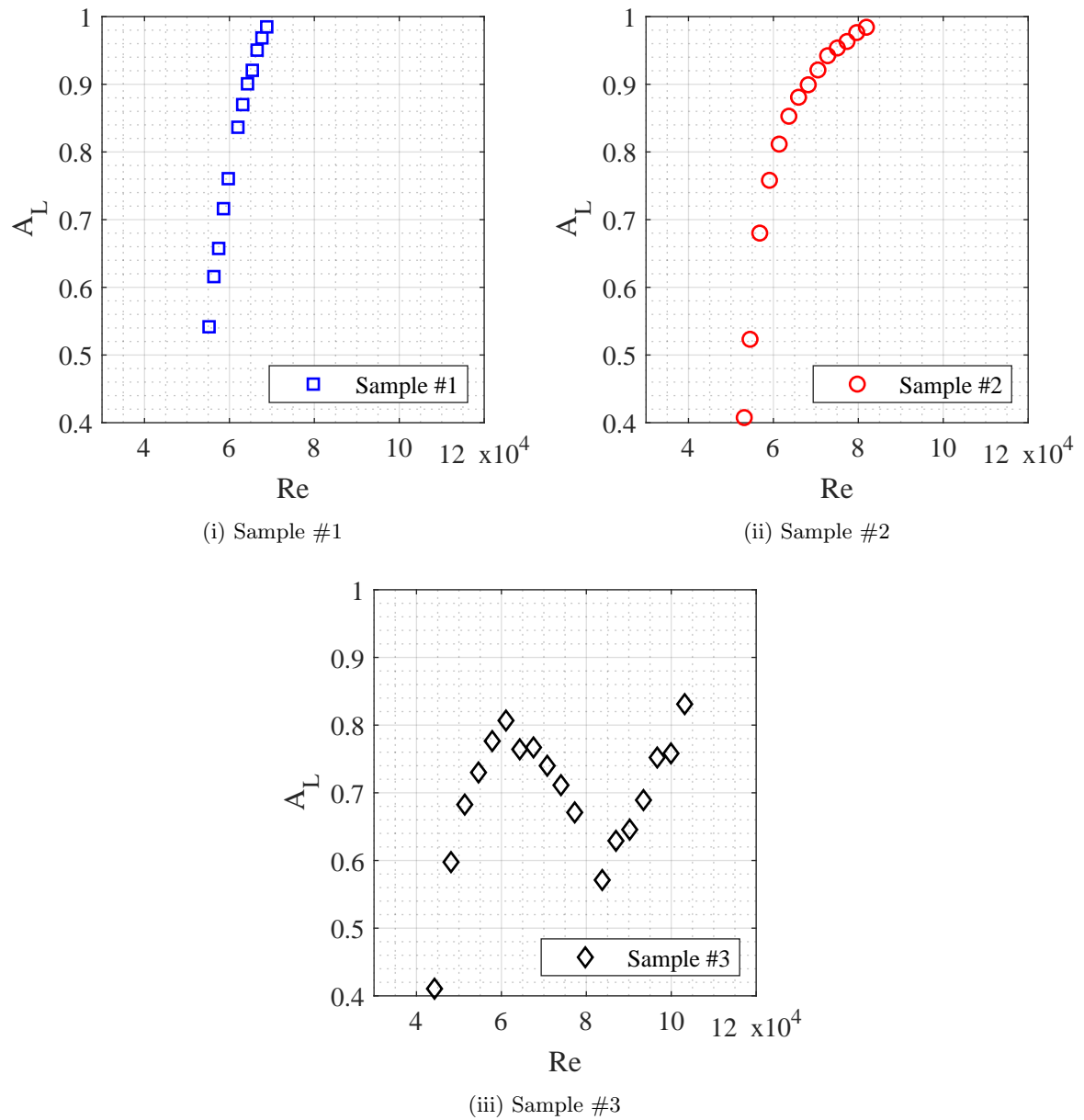
Figure 6.10: The normalized Amplitude of Oscillation by respective length as a function of Reynolds number for samples #1 - 3.

Neck of the flutter shape for the samples with the increasing Re is shown in Figure 6.11, respectively. The growth in neck is similar to that of the growth in the amplitude of oscillation. Furthermore, a linear relationship can be seen when plotted as a function of amplitude of oscillation, as shown in figure 6.12.
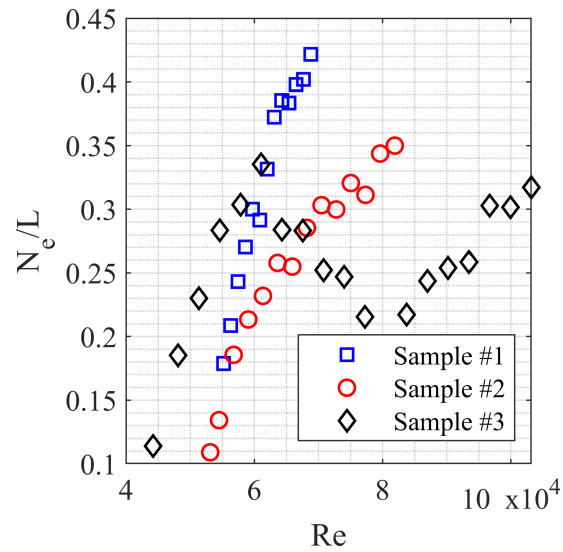
Figure 6.11: The normalized amplitude of neck by respective length as a function of Reynolds number for samples #1 - 3.
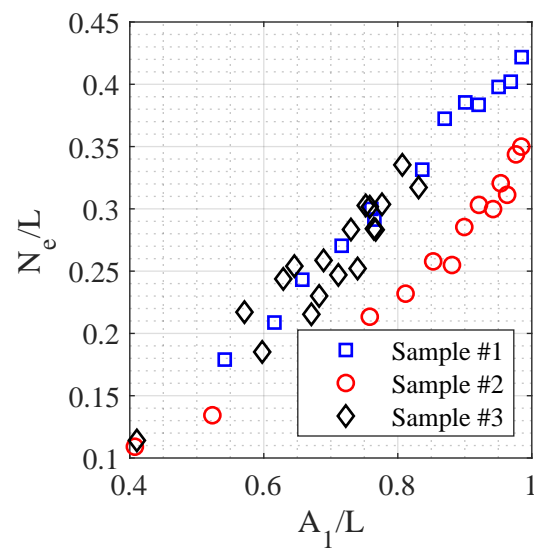
Figure 6.12: The normalized amplitude of neck by respective length as a function of normalized amplitude of oscillation by respective length for samples #1 - 3.

As for the neck, it is only seen for sample #3. This is shown in Figure 6.13 as the neck develops for the increasing Re. Which is also seen to have a linear relationship between the neck growth and the amplitude of oscillation growth shown in Figure 6.14. The comparison of the second amplitude of oscillation and neck to the amplitude of oscillation shows that the flutter mode shape fans out evenly with the increasing velocity source.
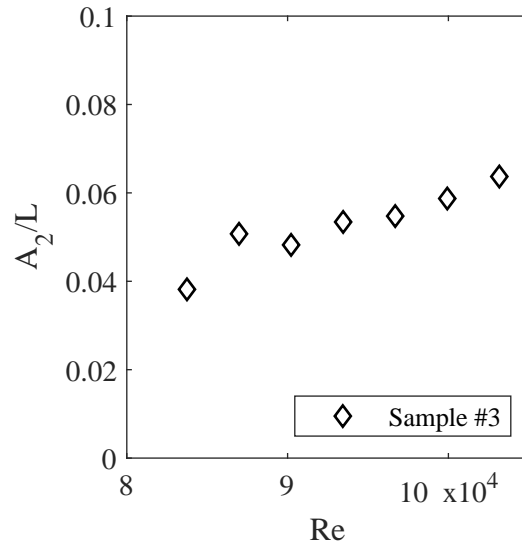
Figure 6.13: The normalized amplitude of neck by respective length as a function of Reynolds number for samples #1 - 3.
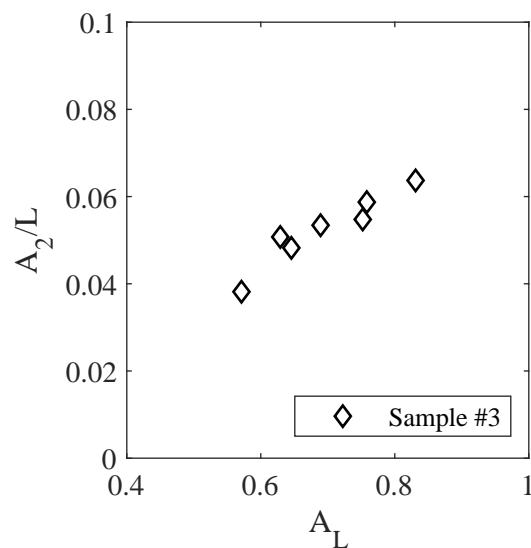
Figure 6.14: The normalized amplitude of neck by respective length as a function of of normalized second amplitude of oscillation by respective length for samples #1 - 3.

The last characteristic that is being compared is the height of the neck location along the y-axis (N_{e_y}) that is normalized by the respective length as a function of Re. This data is plotted in the Figure 6.15. From this, it is apparent that the neck location remains at a constant height for all samples. Flags that flutter at a mode-2 will have a height ratio between 0.4 to 0.6. At the same time, the mode change to mode-3 will have a height ratio of about 0.73.
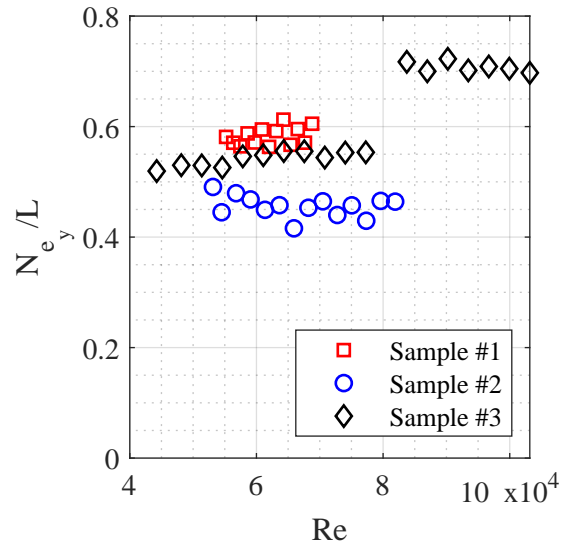
Figure 6.15: The normalized height position of amplitude of neck by respective length as a function of Drag Coefficient for samples #1 - 3.

6.3 FREQUENCY RESPONSE

The auto-spectral density of the time series for the lift is performed to identify dominant frequencies for all the data sets presented. Welch's method in Matlab was used to calculate the auto-spectral density function with a 6000 sample window size with no overlap. A sample of the auto-spectral density for a single set is shown in Figure 6.16, for sample #3 at the Re of $61k$. The dominant frequency is at 25.75 Hz, and its harmonics are also present in this figure. Dominant frequencies are extracted from all the auto-spectral density data sets and are shown in Figure 6.17 as a function of U_∞. A linear relationship is observed for all the samples and a new observation for sample #3, including a new change linear relationships. The curve fit is applied resulting in sample #1 having a slope of 2.34, sample #2 will have a slope of 2.09, and sample #3 will have the slopes of 2.21 for U_∞ values between $8.15(m/s)$ to $14.86(m/s)$ as well as the slope of 4.35 for the U_∞ values between $14.86(m/s)$ to $22.63(m/s)$. As observed before [Taneda, 1968], the slope of the dominant frequency as a function of time is dependent on the material properties. In this case, due to the variation of length, each sample will have a different y-intercept.
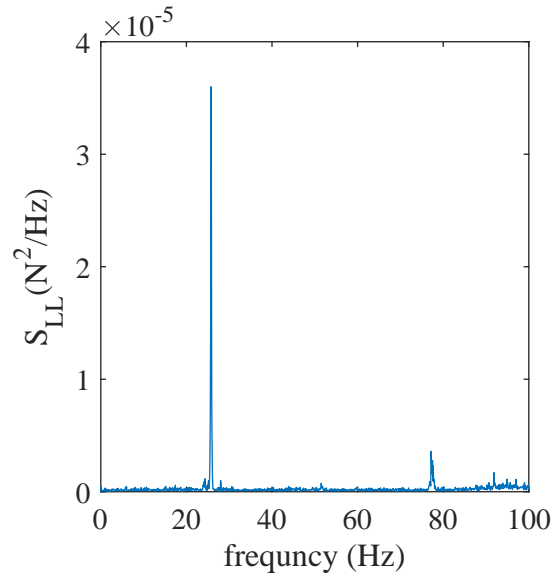
Figure 6.16: The Fast Fourier Transform for sample #3 for the Re of 61k.

The Strouhal number is solved with two separate methods, St_{A_1} with equation 6.2 and St_L with equation 6.3. The St_{A_1} as a function of A_1 normalized by it's respective length is shown in Figure 6.18. Two linear relationships can be observed in this plot. The first will correspond to the flutter behavior for mode-2 indicated with the blue dashed line in the figure with a slope of 0.23. Matching
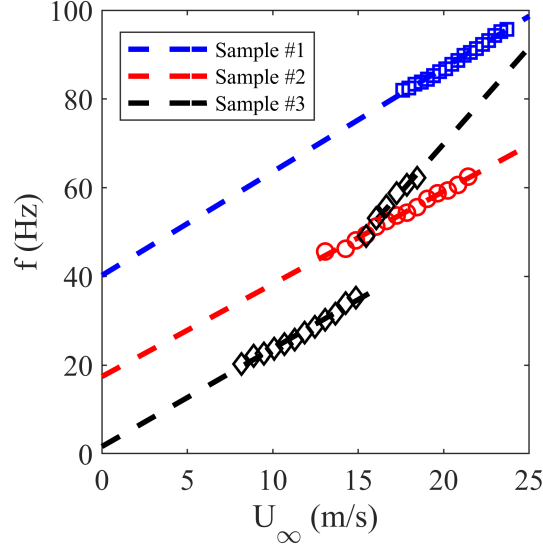
Figure 6.17: The dominant frequency of the flag as a function of inlet velocity for samples #1 - 3.

with several other studies reviewed by Yu [Yu et al., 2019]. The y-intercept will have a zero value since a fluttering frequency of zero will result in no amplitude oscillation value. All three samples will follow this trend except the higher frequencies for sample #2, which begins to trail for the higher amplitudes. The secondary slope arises from the new flutter behavior of the modal changing for sample #3. The new flutter behavior mode-3 flutter has yet to be documented but is shown to have a slope and St_L value of 0.3. Furthermore, the St_L can be shown as a function of Re. The constant St_L of 0.23 is plotted for the red shaded region of mode-2. As for mode-3, it is shown in the blue region.

$$St_{A_1} = \frac{fA_1}{U_\infty} \tag{6.2}$$

$$St_L = \frac{fL}{U_\infty} \tag{6.3}$$

Further knowledge can be gained when St_L is plotted as a function of dimensionless rigidity R_2 which is shown in Figure 6.19. On this figure, several interesting behaviors could be conveyed. Initial mode-2 (M_2) flutter regions could divided two zones shown with a magenta arrow pointing right of the R_2 value of 3.5×10^{-3}. To the left will be the zone for the flutter of mode-3 (M_3). The zone of M_2 could be further sub-divided into the general flag flutter behavior, which is for dimensionless rigidity less than 4.5×10^{-3}, also shown with a red shaded region. The second sub-division is the drag crisis (DC) region which is for dimensionless rigidity from 3.5 to 4.5×10^{-3}, also shown between the two
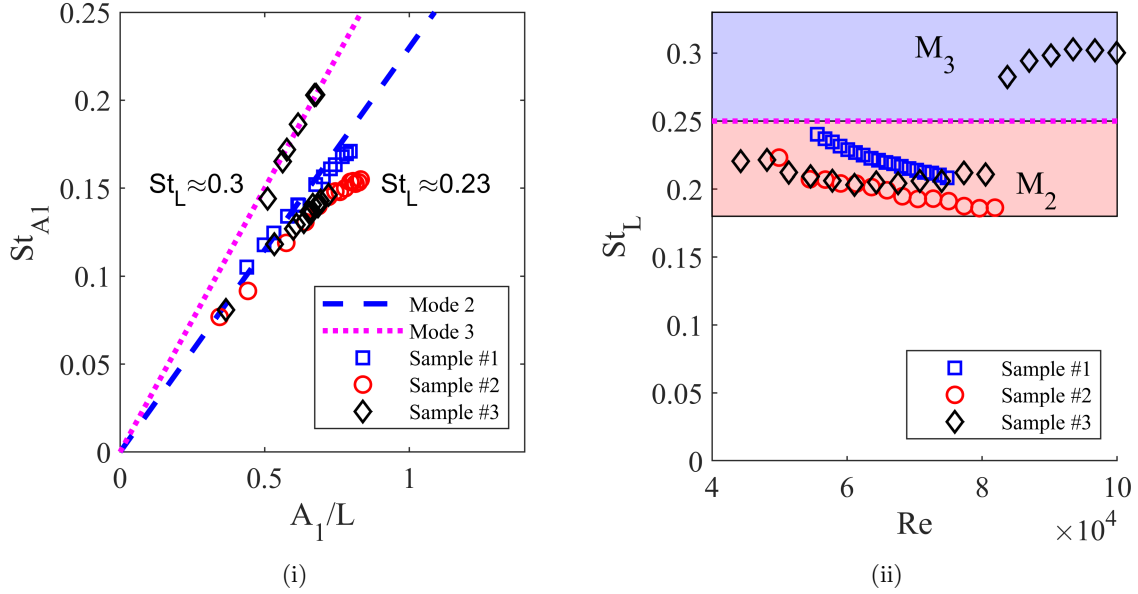
Figure 6.18: The Strouhal number based on the: (i) normalized A_1 by respective length as a function of A_1 and (ii) flag length as a function of Re.

dot-dashed lines in the figure.

These regions are further analyzed, beginning with the general flag flutter region. This region is the most documented but has yet to be compared as such. A positive slope is seen for the three samples presented. The slope for sample #1, shown for the square symbols and a magenta dashed line, is 4.64. For sample #2, the circle symbol and a red dashed line are shown with the slope of 4.50. Finally, sample #3 shows the diamond symbol and blue dashed line, with the slope of 4.40. The slopes of the samples are within the respect of each other with the impact of mass ratio affecting the y-intercept for a single sample. Two different trends are also shown. Comparing sample #1 and sample #2, the slope and y-intercept remains constant but the lower R_2 values of the presented data for sample #1 is the initial for sample #2. As for comparing sample #2 to sample #3, a shift in the y-intercept is experienced. This impact could be better understood in future experiments by spanning the mass ratios to find a proper trend. Furthermore, sample #3 exhibits further changes at the lower R_2. In the drag crisis, sample #3 will experience a change in its initial higher R_2 values trend where the slope turns from positive to negative. Further decreasing the R_2, the DG is overcome by the mode-3 behavior, which causes a sudden spike in the Strouhal number with a larger negative slope. More investigations are needed to understand the new behavior experienced adequately.
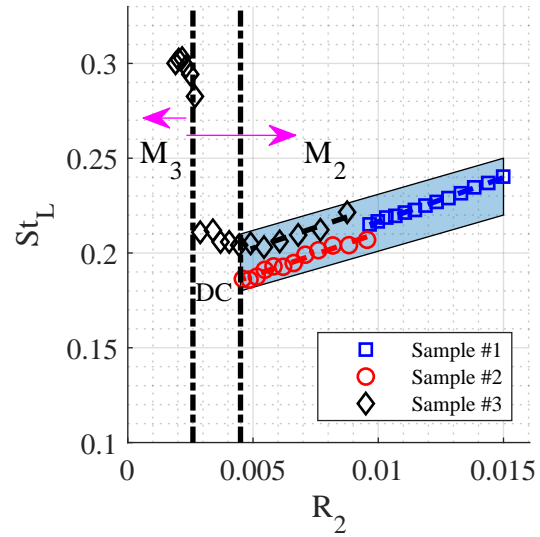
Figure 6.19: The Strouhal number as a function of Dimensionless Rigidity showing: 1) mode-2 (M_2) behavior and 2) mode-3 behavior (M_3).

6.3.1 Drag Coefficient as a function of Amplitude of Oscillation

The C_D could be further analyzed when plotted as a function of the normalized A_1. The new behavior can be highlighted, in which a linear relationship is observed in Figure 6.20. Two distinct regions can be classified as two linear lines, shown in the figure as a magenta dashed line and blue dashed line. Sample #2 and only the mode-2 flutter for sample #3 will follow the magenta curve fit line. The blue dashed line will be followed by sample #1 and the mode-3 flutter for sample #3(shown as blue diamonds). The magenta line will have a slope of 0.2697, while the blue line will have a slope of 0.4254. Thus, two distinct modes of oscillation are observed that depend on the flow regime and flutter behavior. Furthermore, the developing Re value should be considered for sample #3. Initial growth will for the normal flag region have increasing C_D and A_1, but when the flag is in the drag crisis region, the same linear relationship will be followed except with a decrease in C_D and A_1. Upon changing flutter, behavior is experienced from a mode-2 to a mode-3, and the linear relationship will be experienced. This observation is significant as it provides an empirical relationship that can be used to identify the drag experienced by the flexible flag from oscillation amplitude and mode.
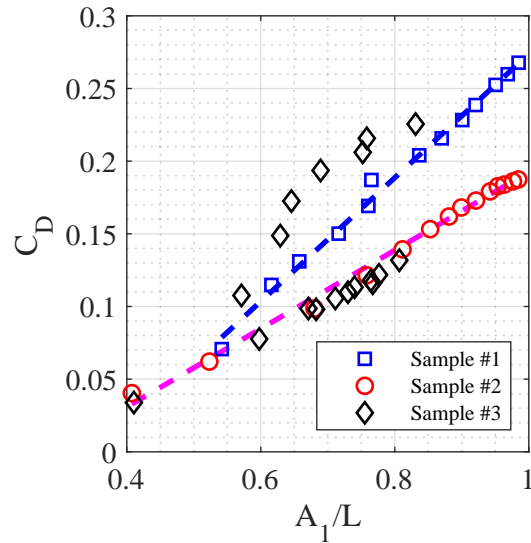
Figure 6.20: The normalized amplitude of oscillation by respective length as a function of Drag Coefficient for samples #1 - 3.

Additional analysis could observed in the drag coefficient (C_D) as a function of the normalized N_e. This relationship is plotted on Figure 6.21. A unique linear relationship is observed and plotted as a blue dashed line. Sample #1, sample #2, and the mode-3 cases for sample #3(shown as blue diamonds) will follow this linear curve fitted line while the mode-2 cases for sample #2 will initially follow this

trend then begin to trail off for the higher Re of the normal flag region and lower Re for the drag crisis region. This blue dashed line will have a slope of 0.7587. The observation will extend the empirical relationship that can be used to identify the drag using the characteristic of the mode shape.
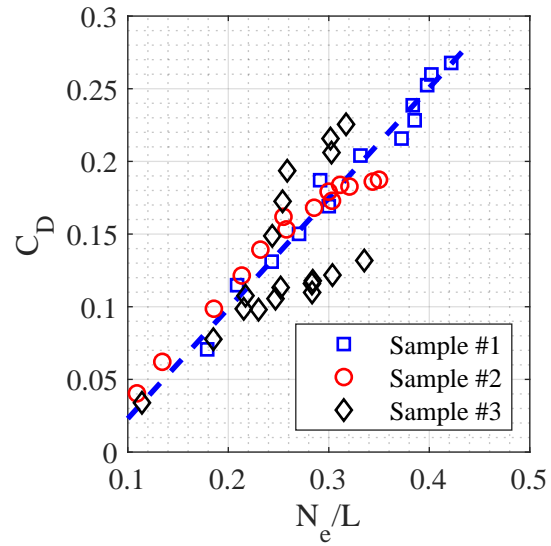
Figure 6.21: The normalized Amplitude of second amplitude of oscillation by respective length as a function of Drag Coefficient for samples #1 - 3.

6.3.2 STABILITY

With the use of the non-dimensional values of R_1 as a function of R_2 a boundary stability was created which is plotted in Figure 6.22. The presented figure is a reduced form of various other instability boundaries [Alben and Shelley, 2008, Shelley and Zhang, 2011, Yu et al., 2019]. The boundary is shown with the black line and a general region, with the upper bound being a stable region for a standard flag and the lower bound being an unstable region. The indicated dash line on Figure 6.22 is in reference to Eloy and Yu, which indicated that initially, flutter would be of mode-2 for R_1 greater than 0.7 [Eloy et al., 2008, Yu et al., 2019]. The mentioned three sample in this paper fall in this region and do in fact initially flutter with a mode-2 as seen in Figure 6.5, 6.6, and 6.7. A dotted line has been added to indicate the region where sample #3 transitions from a mode-2 flutter into a mode-3. Modal changes have been shown in prior studies [Virot et al., 2013] but has yet to be documented and bounded.
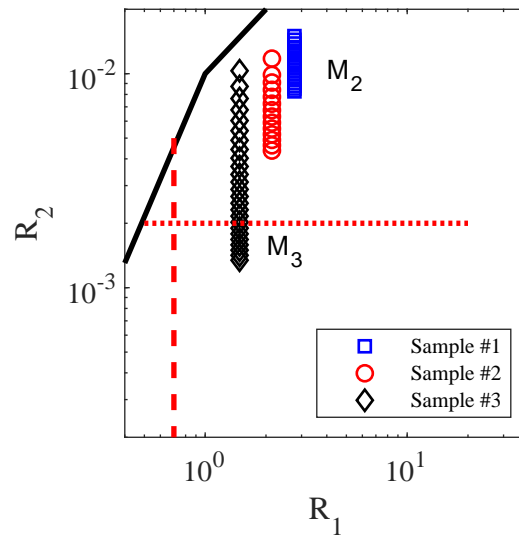
Figure 6.22: The instability boundary layer based on reviewed work [Yu et al., 2019], with unstable region below the black line and stable above. Right of the red dash line is the mode-2 (M_2) region and below the dotted red line is the mode-3 (M_3) region.

6.4 SELECTED CASES

Six cases are shown in the the figure of C_D as a function of Re. These case are selected to compare the along the key non-dimensional values, flutter mode shapes, and velocity fields. Cases (**A**) and (**B**) are individual cases at a Re of 48k and 103k that were used in Section 6.2 to define the flutter characteristics. Case (**C**) is comparing the maximum Re possible for sample #2 with the corresponding Re for sample #3. As for cases (**D**) and (**E**) they are based on the interesting observation for sample #3 at a Re of 61k where a new change in C_D and A_1 is experienced. Results will be presented along with corresponding results for sample #1 and #2. Finally case (**F**) is based on sample #3 at a Re of 90k with corresponding C_D for sample #1 and #2. These cases are overlaid in the Figure 6.23, in which all results for C_D as a function of Re are plotted for ease of comparison.
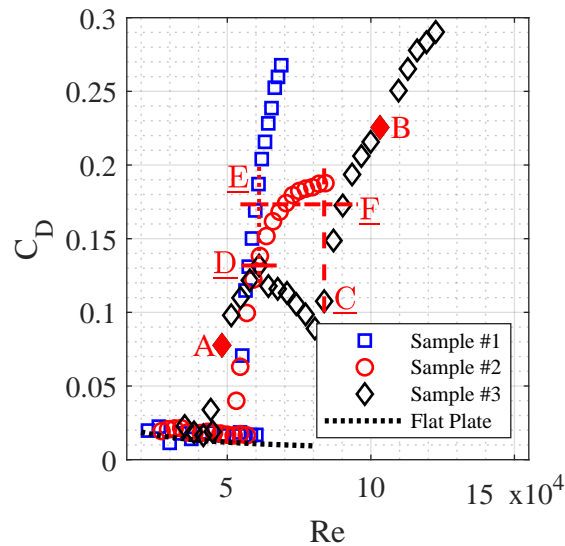
Figure 6.23: Selected case studies based on the C_D as a function of Re.

Based on the cases (**C**), (**D**), (**E**), and (**F**) mentioned in the prior section the superposition of each set as well as key characteristic values and non-dimensional will be compared. Images are created from the superposition average of the imaging study of the flag location for 1000 images over a 77 second period. Each superposition figure is scaled based on the maximum y-axis value experienced in sample #3 and an x-axis value larger than the maximum amplitude of oscillation experienced. The values for all the cases will be summarized in corresponding tables 6.1-6.4.

The first case being analyzed is the case (**C**) which compares the maximum Re achievable for sample #2 with a value of $82k$ with the closest matching Re for sample #3. It is apparent from Figure 6.24 that

sample #2, the left image is fluttering at a mode-2 while sample #3 is fluttering at a mode-3. Though they are the same Re, sample #2 has a larger coefficient of drag, normalized A_1, flutter frequency, and normalized N_e. The list of values are tabulated in table 6.1.

Table 6.1: Non-dimensional values associated to Figure 6.24.

Sample Number	$Re(\times10^3)$	C_D	A_1/L	f Hz	St_A	St_L	N_e/L
#2	82	0.19	0.98	62.5	0.15	0.19	0.35
#3	84	0.11	0.57	49.13	0.14	0.21	0.30
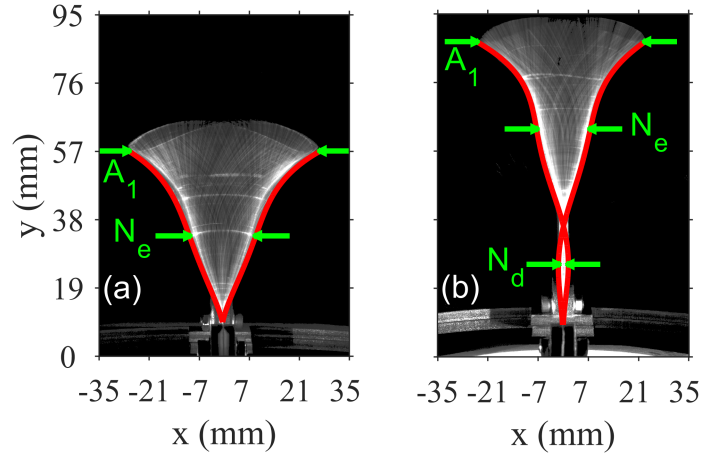
Figure 6.24: The averaged flag flutter for sample #2 (left figure) and sample #3 (right figure). Showing two distinct flutter mode of mode-2 (nodeless) for sample #2 and of mode-3 (single node) for sample #3. This is case (**C**).

Following is case (**D**) which compares the three samples at a C_D of 0.13. For this case, all three samples will be fluttering at a mode-2 as seen in Figure 6.25. In this case, the noticeable similarities are with samples #2 and #3. These two samples experience the same Re, C_D, and normalized A_1. The frequency of sample #2 is also twice that of sample #3. Sample #1 will have a much larger flutter frequency but a smaller normalized A_1 at a lower Re.

Table 6.2: Non-dimensional values associated to Figure 6.25.

Sample Number	$Re(\times10^3)$	C_D	A_1/L	f Hz	St_A	St_L	N_e/L
#1	58	0.13	0.66	83.33	0.14	0.23	0.19
#2	61	0.13	0.81	51.25	0.14	0.2	0.23
#3	61	0.13	0.81	25.75	0.14	0.2	0.31
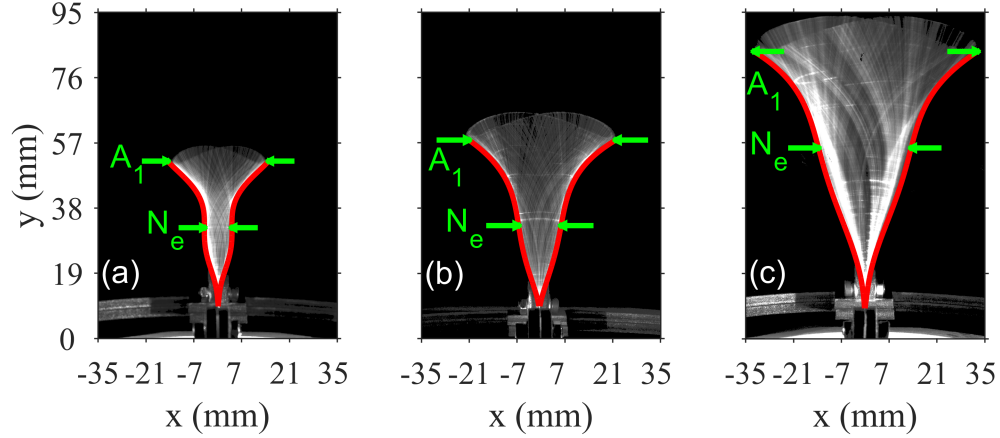
Figure 6.25: The averaged flag flutter sample #1 (left figure), sample #2 (middle figure), and sample #3 (right figure). This is case (**D**) which shows the relation of a local maximum for sample #3 with C_D and A_1/L by comparing the C_D with the other two samples.

Case (**E**) will be a variation of case (**D**), in which sample #3 will have the same Re value as samples #2 and #3. This will in an increase in Re for sample #3 that will have a larger impact of the drag but will have slight changes in the normalized A_1 and flutter frequency.

Table 6.3: Non-dimensional values associated to Figure 6.26.

Sample Number	$Re(\times 10^3)$	C_D	A_1/L	f Hz	St_A	St_L	N_e/L
#1	61	0.19	0.77	85.33	0.15	0.22	0.26
#2	61	0.13	0.81	51.25	0.14	0.2	0.23
#3	61	0.13	0.81	25.75	0.14	0.2	0.31

The last case (**F**) shown in Figure 6.27 compares the three samples at a higher drag value of 0.17 for all three. Notably, sample #3 is at a mode-3 flutter while the other two samples are at a mode-2. Three samples have a variation of Re are experienced to have matching C_D with sample #1 at a value of 60k, sample #2 at a value of 68k, and sample #3 at a value of 90k. This order is reserved about the flutter frequency with sample #1 fluttering at a much higher rate than sample #2 and #3.
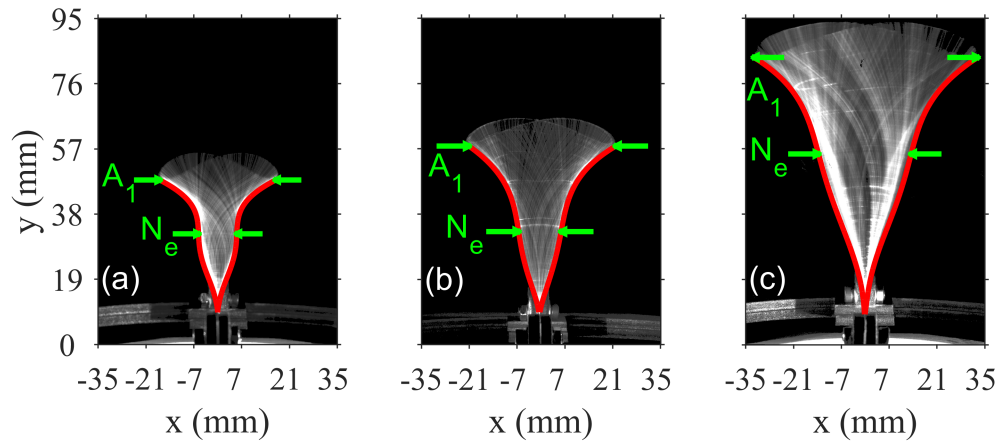
Figure 6.26: The averaged flag flutter sample #1 (left figure), sample #2 (middle figure), and sample #3 (right figure). This is case (**E**) which shows the relation of a local maximum for sample #3 with C_D and A_1/L by comparing the Re with the other two samples.

Table 6.4: Non-dimensional values associated to Figure 6.27.

Sample Number	$Re(\times10^3)$	C_D	A_1/L	f Hz	N_e/L
#1	60	0.17	0.76	84.50	0.23
#2	68	0.17	0.89	54.38	0.34
#3	90	0.17	0.65	51.24	0.29
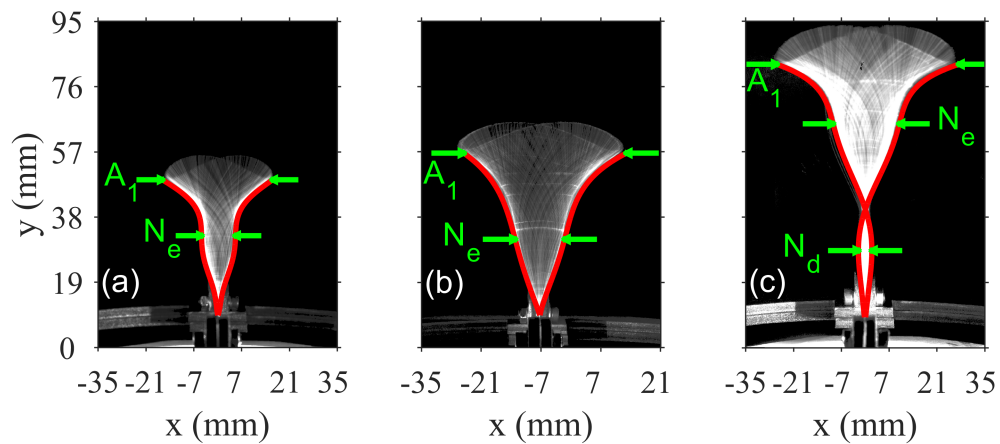
Figure 6.27: The averaged flag flutter sample #1 (left figure), sample #2 (middle figure), and sample #3 (right figure). This is case (**F**) which shows the relation of a local maximum for sample #3 with C_D and A_1/L by comparing the Re with the other two samples.

6.5 AVERAGED VELOCITY FIELD

This section shows the average of the resulting PIV image per experimental run for the cases in the section Flag Location. One thousand images were used to acquire for a single velocity field but are best shown based on their velocity components. This is done by showing U_x and U_y velocity field components separately for each case. The axis has been adjusted to show as much of the wake region as possible. The wake region will correspond to the larger y values. In this wake region, for the region of positions great than x = 20 and lower than x = -20, a change in velocity is seen. This region is the shear layer zone. For reference, upstream is considered $y = 0$ and downstream is considered $y = 100$. An area at the inlet was also blocked off due to high-level uncertainties from the imaging of the flag stand that is located at $(0, 0)$. The non-dimensional values refereed in the table 6.1-6.4 in the section of Flag Location will be the same for the respective cases.

The first presented case is the case (**B**) which compares a sample #2 at mode-2 flutter with a sample #3 at mode-3 flutter with both at a Re around 82k. Similar conditions are observed when the area in the A_2 region for a mode-3 flutter is ignored. From Figure 6.5(i), we can notice similar wake U_x on average for a model 2 and a mode-3 flutter. This could be divided into two sections about the y-axis at $x = 0$, for the region where $x < 0$, a negative U_x that begins at $y = 35$, which is well under the location of the trailing edge. Just upstream of this region, the outline of the shape of averaged flag location is observed. This will have a negative U_x value. The contrast is seen in the region where $x > 0$, which has a positive U_x value, and the area near the averaged flag location will experience a negative U_x. While the flag flutters, one can decipher that the inlet flow will cause fluid to displace outward in the wake, which is dominated by the flag motion. The final notable region in Figure 6.28i is the A_2 region for sample #3, which would be around the coordinate (0,10) in the image (b). At this region, there is no U_x which suggests, on average, this region does not experience much fluid motion in the x-direction.

Further observation could be made from Figure 6.28ii and the U_y components could be analyzed. Similar to the prior figure, division into two sections about the y-axis where $x = 0$ could be done, but the regions will be symmetrical about the axis rather than opposites. In the wake region, the area that flows near the middle will be similar to inlet conditions as the x-positions shift away from zero, the U_y will decrease. The area closer to the inlet, near the coordinates $(17, 65)$, shows a decrease in velocity at the flag location. This decrease in velocity will be due to the blockage of the inlet flow when the flag is at the extremes. Then the area at the center of the flag location, at the center region $(0, 55)$, the velocity experiences an increase compared to the inlet velocity. This is due to the motion of the flag in this region, causing the flow to accelerate. Lastly in the A_2 region, located at about the coordinate

$(0, 15)$, will experience a velocity decrease. This is due to the A_2 having a small amount of motion, obstructing the flow.
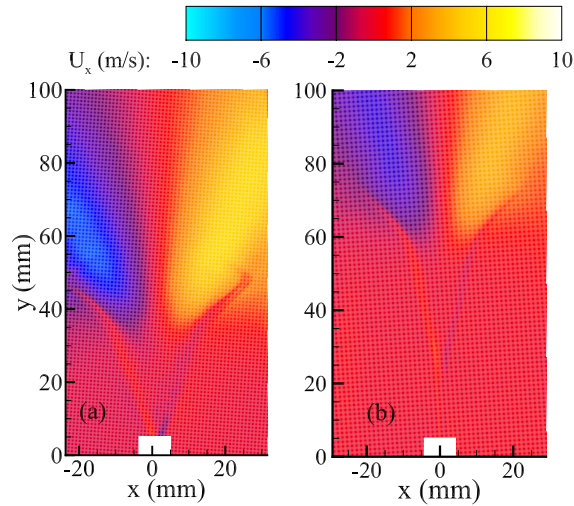
(i) U_x component velocity field.
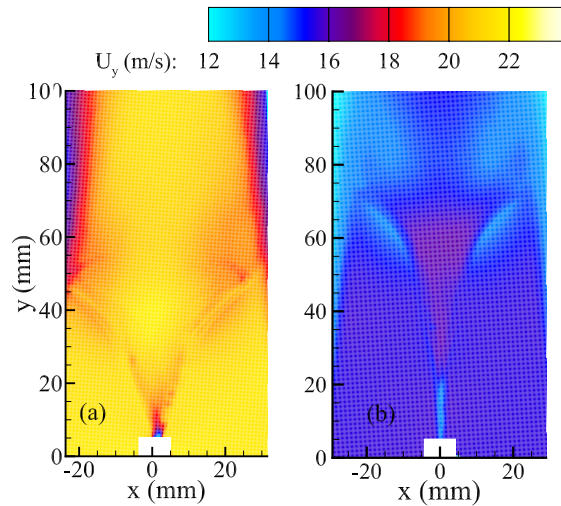
(ii) U_y component velocity field.

Figure 6.28: The averaged velocity field of case (**C**), Figure 6.24, of 1000 PIV images for the velocity components: Images (i) U_x of and Images (ii) U_y.

The following figure 6.29i and 6.29ii are the averaged velocity field for case (**D**). Which compares the three samples at a constant C_D value of 0.13. For all these, they are in mode-2 but do not experience anything different on average compared to the sample #2 in the last case (**C**). The same behavior is observed except with variations of velocities. This suggests that the mode flutter influences the flow

field rather than the flag geometry.

(i) U_x component velocity field.

(ii) U_y component velocity field.

Figure 6.29: The averaged velocity field of case (**D**), Figure 6.25, of 1000 PIV images for the velocity components: Image (a) U_x of and Image (b) U_y. Corresponding to figure 6.24.

When a single Re is changed for a single sample, which is the difference between case (**D**) and (**E**) since the only Re changed in sample #3 going from a Re of 58k to 61k. The only difference seen in that case (**E**) will change would be the shape of the flag location region. This is observed when comparing Figure 6.30i and 6.30ii. The blockage region will expand outward since the amplitude is increasing. All other highlighted regions will be similar.

U$_x$ (m/s): -10   -8   -6   -4   -2   0   2   4   6   8   10

(i) U_x component velocity field.

U$_y$ (m/s): 10   11   12   13   14   15   16   17   18   19   20
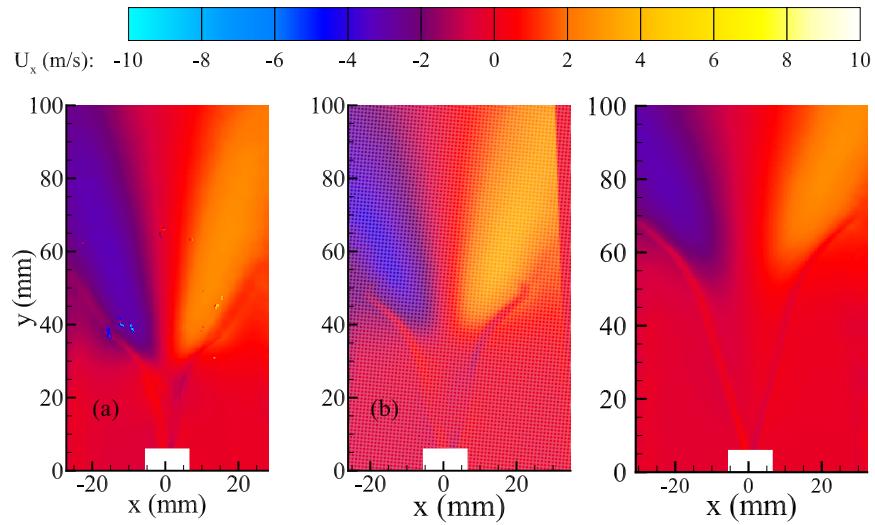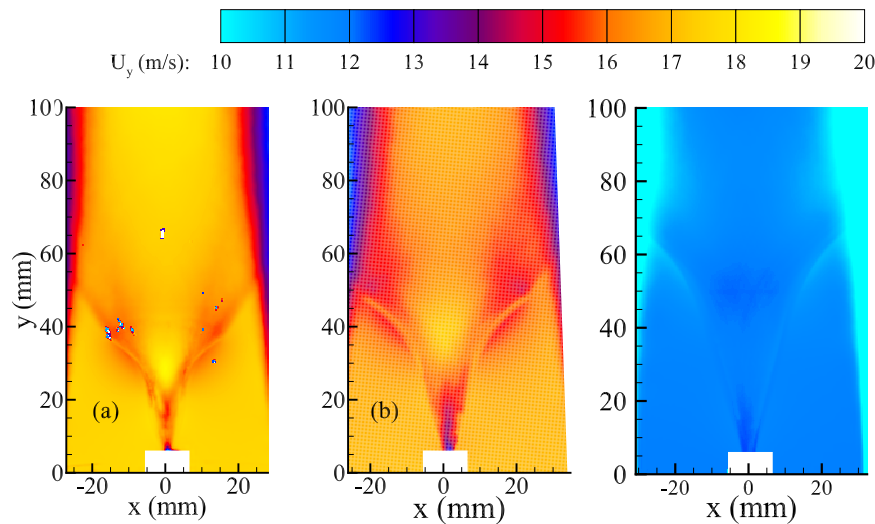
(ii) U_y component velocity field.

Figure 6.30: The averaged velocity field of case (**E**), Figure 6.26, of 1000 PIV images for the velocity components: Image (a) U_x of and Image (b) U_y. Corresponding to figure 6.26.

In figure 6.27, the final case (**F**) then compares the similar C_D of 0.17 for all three samples. The flag location region mentioned for samples #1 and #2, which are images (a) and (b), respectively, only show a shift of the blockage region due to the amplitude growth. While sample #3, which is in a mode-3 flutter, has similar A_2, flutter, and wake regions to those in case (**C**). The difference is case (**F**) has a higher Re. The regions are more pronounced in this case due to this fact.

(i) U_x component velocity field.

(ii) U_y component velocity field.
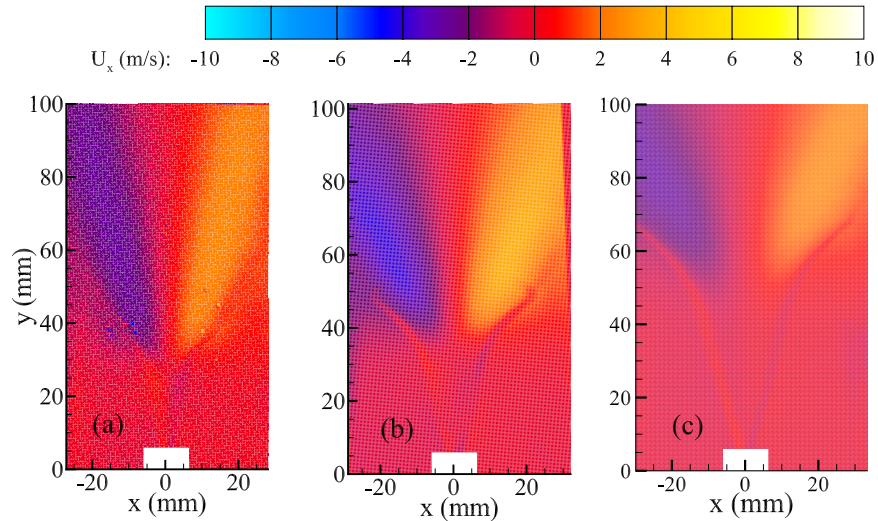
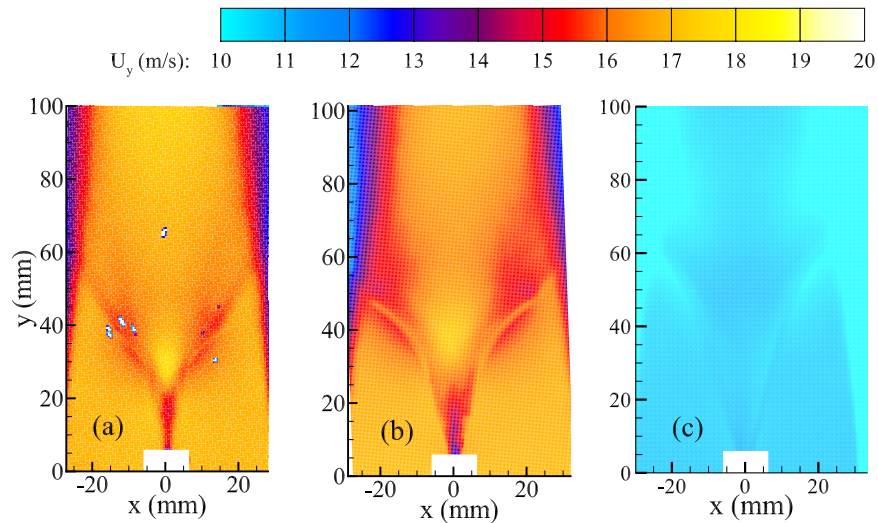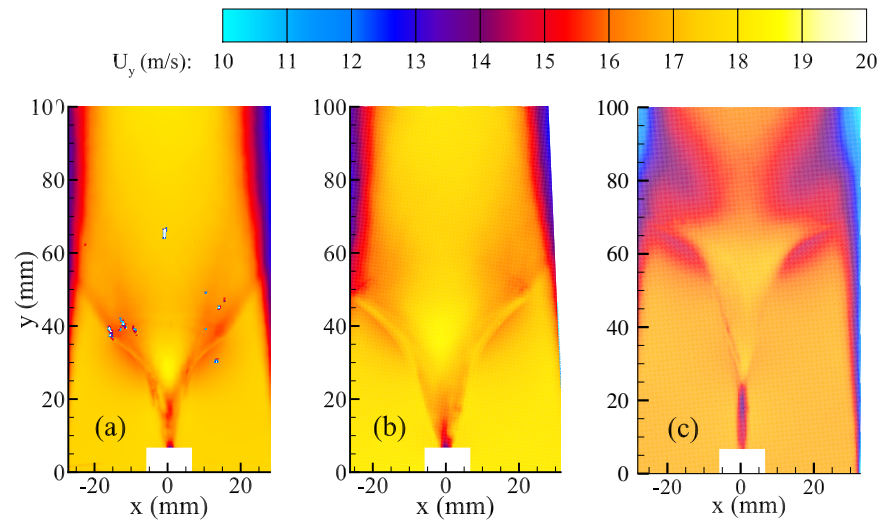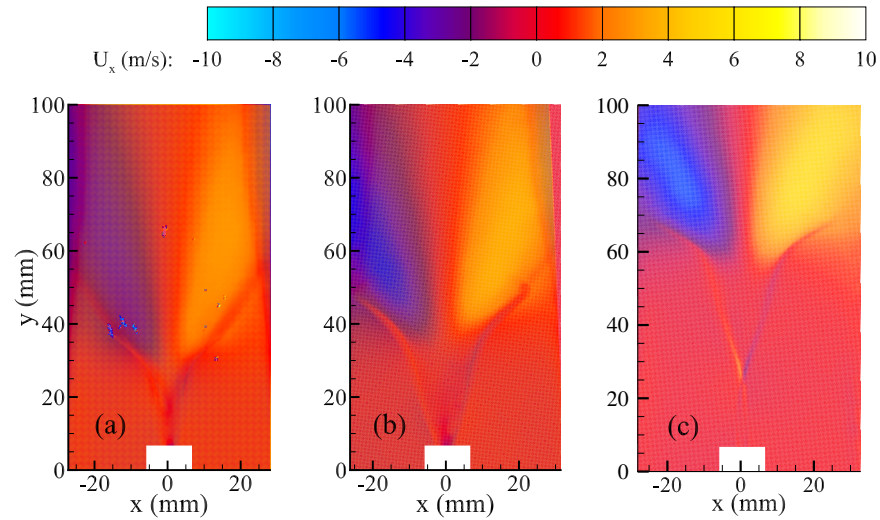Figure 6.31: The averaged velocity field of case (**F**), Figure 6.27, of 1000 PIV images for the velocity components: Image (a) U_x of and Image (b) U_y. Corresponding to Figure 6.27.

Chapter 7: Summary and Conclusions

Experiments were performed to study the aerodynamics and FSI behavior of three different flags. All the experiments were conducted at the University of Idaho's Experimental Fluids and Aerodynamic Laboratory. A load cell was used to quantify the aerodynamic measurements experienced by the flag during fluttering, flag images were used to characterize its fluttering, and a PIV was used to quantify the velocity around the flag. The key non-dimensional for the flag FSI behavior are the mass ratio (R_1), dimensionless rigidity (R_2), and Reynolds number (Re). Samples #1, #2, and #3 have the R_1 values of: 2.77, 2.14 and 1.48, respectively. For this study R_2 varied from $1.3 \times 10^{-3} to 14.5 \times 10^{-3}$, and Re varied from 44×10^3 to 123×10^3.

The aerodynamic measurements show unique drag characteristics for the membrane and is dependent on R_1, R_2, and Re. The aerodynamic results show an increase in the drag coefficient with the increase in Re for samples #1 and 2. For the flag sample#3, we observe an initial increase in drag with an increase in Re, followed by a decrease in drag with an increase in Re, referred to as a drag crisis region. A further increase in the Re value, a sharp increase in the drag referred to as the drag recovery region is observed for the sample#3. A similar trend is also observed for varying R_2. The aerodynamic results demonstrated the bifurcation with lower and upper bounds of the critical velocities for all three flag samples.

Images of the superimposed flag were used to characterize the flag flutter behavior. These results showed that the presented flag problem has two distinct modes of oscillations modes 2 and 3. The mode-2 behavior is observed for all three flag samples and while the mode-3 behavior is only observed for flag sample#3 at higher Re values. A distinct feature for mode 3 is the presence of A_2 in the flag oscillations. For the mode-2 oscillations, an increase in oscillation amplitudes is observed with an increase in Re for samples #1 and #2. For sample# 3, similar behavior is initially experienced, followed by a decrease in the oscillation amplitude with the increase in Re except for the drag crisis region. The drag recovery region for sample# 3 shifts to mode-3 oscillation with a further increase in the Re. The flag images show that the neck region observed in mode-2 and mode-3 does not move but grows in amplitude. The amplitude of oscillation and neck oscillation will also grow linearly with the increasing Re. These results suggest that the membrane amplitude is fan out evenly. Further emphasizing that the drag is dependent on the coherent shape and the frequency at which the membrane flutters.

Auto-spectral density function is used to acquire the dominant frequency of the aerodynamic load. The Strouhal number based on the dominant frequency, u_∞, and membrane length vary depending on the current oscillating mode. For example, for mode-2 flutter, the Strouhal number has a value of 0.2,

while for mode-3, the Strouhal number has a value of 0.3. This suggests that the mode change is associated with a shift in dominant frequency.

The averaged velocity field results clearly show the difference between the averaged mode-2 and mode-3 flutter. Both the oscillation modes will cause the inlet flow to spread outward from the centerline of the jet outlet in the wake region caused by membrane motion. The average velocity results show the highest velocity point at the center of the coherent flutter shape, the most energized region. The A_2, a key feature of mode-3 oscillations, can also be observed in the average velocity results. The A_2 region will have very little motion compared to the region above the A_2, as evident from low values of U_x and U_y components of velocity.

Conducting these experiments and analyzing the data of the FSI flag problem has provided empirical data that aids in further understanding the physical development of the flag and the aerodynamic performance. Insight is provided in linear relationship of the amplitude grow to drag generated due to flutter. Advanced data techniques were employed to gain insight on the fluid field surrounding the flutter flag for several modal cases and unique phenomenon such as in stages of modal change. However, due to the complexity of the problem, other advanced measurement techniques and analysis must be employed on unique phenomena such as bifurcation, modal change, and chaotic flutter. Furthermore, several future works can arise from the presented data.

Chapter 8: Future Work

8.1 Changing Geometry

Due to the lack of reported experimental work in membranes that will experience mode changes, there is an interest in selecting geometries that will experience the phenomenon. For this reason the thickness will be varied for Sample #3 to see the affects. Varying the thickness will change the mass ratio and the dimensionless rigidity. This will be varying locations on the boundary stability plot while still retaining the same phenomenons experienced in Sample #3. All analysis shown in the study can be replicated for these cases, as well as future indepth and advanced intended experimental and analysis techniques.

8.2 Near Wall Analysis

The near wall dynamics of the flag has yet to be properly addressed for various flutter modes or for the complete limit cycle. particle image velocimetry (PIV) studies have been conducted for a mode 2 flutter showing the flow near the wall for the flutter membranes in upstroke and downstroke conditions [Gibbs et al., 2014]. It shows that the flow did not separate for these conditions. The bifurcation region has yet to be analyzed by means of PIV or other experimental techniques that allow for near wall studies. As well as cases for transition for mode changes and higher order mode values.

8.3 Wake Analysis

As the membrane flutters a Von-Karman vortex street and Kelvin-Helmholtz instability has been identified to shed from at the free end [Zhang et al., 2000]. Though it has yet to be qualified experimentally at what frequency shedding is seen to occur. The shedding can be measured through precisely controlled experimental studies employing a Hot-Wire Anemometry and a method to track the location of the membrane with time-series. This could be done by spanning the wake area to generate a complete wake profile. Interesting cases could be selected based on bifurcation, mode flutter, and transition phases.

8.4 Advance Analysis: POD and DMD

Large data sets for PIV studies have been collected for all the samples mentioned at all the varying Re. With these data sets, the advanced data analysis such as Proper Orthogonal Decomposition (POD) and Dynamic Mode Decomposition (DMD), can be applied to determine the spatial and temporal

behavior of the surrounding fluid for the fluttering membrane. These are data driven decomposition techniques that can be applied to the data collected from PIV results. These techniques can be used to identify the optimal "modes" or basis function which are the eigenmodes of the equation. With this the velocity field can be reconstructed that in turn can estimate the pressure field that can help better understand the fluid loading and membrane motion.

8.5 Modeling Membrane and Fluid Interaction

Data driven modeling can be done that will comply with all the phenomenon captured with the experimental data. This could be done with the methods explained in the background section including: theoretical linear stability, linear/nonlinear vortex lattice model, coupled fluid-structure direct simulation, or immersed boundary method. Several other approaches can also be implemented such as "Deep Galerkin Method (DGM)" [Sirignano and Spiliopoulos, 2018]. This approach uses neutral networks to implement Deep Learning to solve high-dimensional partial differential equations(PDE). This has yet to be applied to solve two PDE's.

References

[Alben and Shelley, 2008] Alben, S. and Shelley, M. J. (2008). Flapping states of a flag in an inviscid fluid: bistability and the transition to chaos. *Physical review letters*, 100(7):074301.

[Argentina and Mahadevan, 2005] Argentina, M. and Mahadevan, L. (2005). Fluid-flow-induced flutter of a flag. *Proceedings of the National Academy of Sciences*, 102(6):1829–1834.

[Augier et al., 2012] Augier, B., Bot, P., Hauville, F., and Durand, M. (2012). Experimental validation of unsteady models for fluid structure interaction: Application to yacht sails and rigs. *Journal of Wind Engineering and Industrial Aerodynamics*, 101:53–66.

[Bottai et al., 2019] Bottai, A. M., Jonson, M. L., and Campbell, R. L. (2019). *Investigation of the role of higher order torsion & bending modes in flutter stability for flexible slender wings.*

[Carruthers and Filippone, 2005] Carruthers, A. and Filippone, A. (2005). Aerodynamic drag of streamers and flags. *Journal of aircraft*, 42(4):976–982.

[Cavolowsky, 2017] Cavolowsky, J. A. (2017). Advanced aerodynamic design center for ultra-efficient commercial vehicles.

[Chen et al., 2014] Chen, M., Jia, L.-B., Wu, Y.-F., Yin, X.-Z., and Ma, Y.-B. (2014). Bifurcation and chaos of a flag in an inviscid flow. *Journal of Fluids and Structures*, 45:124–137.

[Chun-Yu et al., 2010] Chun-Yu, B., Chao, T., Xie-Zhen, Y., and Xi-Yun, L. (2010). Flutter of finite-span flexible plates in uniform flow. *Chinese Physics Letters*, 27(6):064601.

[Cisonni et al., 2017] Cisonni, J., Lucey, A. D., Elliott, N. S., and Heil, M. (2017). The stability of a flexible cantilever in viscous channel flow. *Journal of Sound and Vibration*, 396:186–202.

[Connell and Yue, 2007] Connell, B. S. and Yue, D. K. (2007). Flapping dynamics of a flag in a uniform stream. *Journal of fluid mechanics*, 581:33.

[Dhawan, 1991] Dhawan, S. (1991). Bird flight. *Sadhana*, 16(4):275–352.

[Dowell, 1970] Dowell, E. H. (1970). Panel flutter-a review of the aeroelastic stability of plates and shells. *AIAA journal*, 8(3):385–399.

[Eloy et al., 2012] Eloy, C., Kofman, N., and Schouveiler, L. (2012). The origin of hysteresis in the flag instability. *Journal of fluid mechanics*, 691:583–593.

[Eloy et al., 2008] Eloy, C., Lagrange, R., Souilliez, C., and Schouveiler, L. (2008). Aeroelastic insta-bility of cantilevered flexible plates in uniform flow. *arXiv preprint arXiv:0804.0774.*

[Eloy et al., 2007] Eloy, C., Souilliez, C., and Schouveiler, L. (2007). Flutter of a rectangular plate. *Journal of fluids and structures*, 23(6):904–919.

[Fairthorne, 1930] Fairthorne, R. A. (1930). Drag in flags. *Aeronautical Research Committee, Reports, and Memorandum.*, 1345:887–891.

[Favier et al., 2014] Favier, J., Revell, A., and Pinelli, A. (2014). A lattice boltzmann–immersed bound-ary method to simulate the fluid interaction with moving and slender flexible objects. *Journal of Computational Physics*, 261:145–161.

[Gallegos and Sharma, 2017] Gallegos, R. K. B. and Sharma, R. N. (2017). Flags as vortex generators for heat transfer enhancement: Gaps and challenges. *Renewable and Sustainable energy reviews*, 76:950–962.

[Giacomello and Porfiri, 2011] Giacomello, A. and Porfiri, M. (2011). Underwater energy harvesting from a heavy flag hosting ionic polymer metal composites. *Journal of Applied Physics*, 109(8):084903.

[Gibbs et al., 2014] Gibbs, S., Fichera, S., Zanotti, A., Ricci, S., and Dowell, E. H. (2014). Flow field around the flapping flag. *Journal of Fluids and Structures*, 48:507–513.

[Goland, 1945] Goland, M. (1945). The flutter of a uniform cantilever wing.

[Goza and Colonius, 2018] Goza, A. and Colonius, T. (2018). Modal decomposition of fluid–structure interaction with application to flag flapping. *Journal of Fluids and Structures*, 81:728–737.

[Haghighat et al., 2012] Haghighat, S., Martins, J. R., and Liu, H. H. (2012). Aeroservoelastic design optimization of a flexible wing. *Journal of Aircraft*, 49(2):432–443.

[Herrault et al., 2012] Herrault, F., Hidalgo, P., Ji, C.-H., Glezer, A., and Allen, M. (2012). Cooling performance of micromachined self-oscillating reed actuators in heat transfer channels with integrated diagnostics. In *2012 IEEE 25th International Conference on Micro Electro Mechanical Systems (MEMS)*, pages 1217–1220. IEEE.

[Howell et al., 2009] Howell, R., Lucey, A., Carpenter, P., and Pitman, M. (2009). Interaction between a cantilevered-free flexible plate and ideal flow. *Journal of Fluids and Structures*, 25(3):544–566.

[Huang, 1995] Huang, L. (1995). Flutter of cantilevered plates in axial flow. *Journal of Fluids and Structures*, 9(2):127–147.

[Huang and Sung, 2010] Huang, W.-X. and Sung, H. J. (2010). Three-dimensional simulation of a flapping flag in a uniform flow. *Journal of Fluid Mechanics*, 653:301.

[Ifju et al., 2002] Ifju, P., Jenkins, D., Ettinger, S., Lian, Y., Shyy, W., and Waszak, M. (2002). Flexible-wing-based micro air vehicles. In *40th AIAA aerospace sciences meeting & exhibit*, page 705.

[Jia et al., 2007] Jia, L.-B., Li, F., Yin, X.-Z., and Yin, X.-Y. (2007). Coupling modes between two flapping filaments. *Journal of Fluid Mechanics*, 581:199.

[Jia et al., 2018] Jia, Y., Jia, L., Su, Z., and Yuan, H. (2018). Experimental investigation of flow field around the elastic flag flapping in periodic state. *Modern Physics Letters B*, 32(12n13):1840031.

[Jiakun et al., 2020] Jiakun, H., Zhe, H., Fangbao, T., and Gang, C. (2020). Review on bio-inspired flight systems and bionic aerodynamics. *Chinese Journal of Aeronautics*.

[Kim et al., 2013] Kim, D., Cossé, J., Cerdeira, C., and Gharib, M. (2013). Flapping dynamics of an inverted flag. *Journal of Fluid Mechanics*.

[Lee et al., 2018] Lee, J. B., Park, S. G., and Sung, H. J. (2018). Heat transfer enhancement by asymmetrically clamped flexible flags in a channel flow. *International Journal of Heat and Mass Transfer*, 116:1003–1015.

[Lemaitre et al., 2005] Lemaitre, C., Hémon, P., and De Langre, E. (2005). Instability of a long ribbon hanging in axial air flow. *Journal of Fluids and Structures*, 20(7):913–925.

[Li and Lipson, 2009] Li, S. and Lipson, H. (2009). Vertical-stalk flapping-leaf generator for wind energy harvesting. In *Smart materials, adaptive structures and intelligent systems*, volume 48975, pages 611–619.

[Loring, 1941] Loring, S. J. (1941). General approach to the flutter problem. *SAE Transactions*, pages 345–356.

[Martin, 2006] Martin, A. H. (2006). *Experimental study of drag from a fluttering flag*. PhD thesis, Oklahoma State University.

[Mei et al., 1999] Mei, C., Abdel-Motagaly, K., and Chen, R. (1999). Review of nonlinear panel flutter at supersonic and hypersonic speeds.

[Michelin and Llewellyn Smith, 2009] Michelin, S. and Llewellyn Smith, S. G. (2009). Resonance and propulsion performance of a heaving flexible wing. *Physics of Fluids*, 21(7):071902.

[Molki and Breuer, 2010] Molki, M. and Breuer, K. (2010). Oscillatory motions of a prestrained compliant membrane caused by fluid–membrane interaction. *Journal of fluids and structures*, 26(3):339–358.

[Morris-Thomas and Steen, 2009] Morris-Thomas, M. T. and Steen, S. (2009). Experiments on the stability and drag of a flexible sheet under in-plane tension in uniform flow. *Journal of Fluids and Structures*, 25(5):815–830.

[NASA, 2021] NASA (2021). Green aviation.

[Orrego et al., 2017] Orrego, S., Shoele, K., Ruas, A., Doran, K., Caggiano, B., Mittal, R., and Kang, S. H. (2017). Harvesting ambient wind energy with an inverted piezoelectric flag. *Applied energy*, 194:212–222.

[Païdoussis, 1998] Païdoussis, M. P. (1998). *Slender structures and axial flow*, volume 1. Elsevier.

[Pan et al., 2014] Pan, D., Shao, X., Deng, J., and Yu, Z. (2014). Simulations of passive oscillation of a flexible plate in the wake of a cylinder by immersed boundary method. *European Journal of Mechanics-B/Fluids*, 46:17–27.

[Pang et al., 2010] Pang, Z., Jia, L.-b., and Yin, X.-z. (2010). Flutter instability of rectangle and trapezoid flags in uniform flow. *Physics of Fluids*, 22(12):121701.

[Peterson et al., 1996] Peterson, C., Strickland, J., and Higuchi, H. (1996). The fluid dynamics of parachute inflation. *Annual Review of Fluid Mechanics*, 28(1):361–387.

[Raffel et al., 2018] Raffel, M., Willert, C. E., Scarano, F., Kähler, C. J., Wereley, S. T., and Kompenhans, J. (2018). *Particle image velocimetry: a practical guide*. Springer.

[Rojratsirikul et al., 2010] Rojratsirikul, P., Wang, Z., and Gursul, I. (2010). Unsteady fluid-structure interactions of membrane airfoils at low reynolds numbers. In *Animal Locomotion*, pages 297–310. Springer.

[Sane, 2003] Sane, S. P. (2003). The aerodynamics of insect flight. *Journal of experimental biology*, 206(23):4191–4208.

[Sarpkaya, 1979] Sarpkaya, T. (1979). Vortex-induced oscillations: a selective review.

[Sfakiotakis et al., 1999] Sfakiotakis, M., Lane, D. M., and Davies, J. B. C. (1999). Review of fish swimming modes for aquatic locomotion. *IEEE Journal of oceanic engineering*, 24(2):237–252.

[Shelley et al., 2005] Shelley, M., Vandenberghe, N., and Zhang, J. (2005). Heavy flags undergo spontaneous oscillations in flowing water. *Physical review letters*, 94(9):094302.

[Shelley and Zhang, 2011] Shelley, M. J. and Zhang, J. (2011). Flapping and bending bodies interacting with fluid flows. *Annual Review of Fluid Mechanics*, 43:449–465.

[Shi et al., 2013] Shi, S., New, T., and Liu, Y. (2013). Flapping dynamics of a low aspect-ratio energy-harvesting membrane immersed in a square cylinder wake. *Experimental Thermal and Fluid Science*, 46:151–161.

[Sirignano and Spiliopoulos, 2018] Sirignano, J. and Spiliopoulos, K. (2018). Dgm: A deep learning algorithm for solving partial differential equations. *Journal of computational physics*, 375:1339–1364.

[Stein et al., 2000] Stein, K., Benney, R., Kalro, V., Tezduyar, T. E., Leonard, J., and Accorsi, M. (2000). Parachute fluid–structure interactions: 3-d computation. *Computer Methods in Applied Mechanics and Engineering*, 190(3-4):373–386.

[Taneda, 1968] Taneda, S. (1968). Waving motions of flags. *Journal of the Physical Society of Japan*, 24(2):392–401.

[Tang et al., 2015] Tang, C., Liu, N.-S., and Lu, X.-Y. (2015). Dynamics of an inverted flexible plate in a uniform flow. *Physics of Fluids*, 27(7):073601.

[Tang et al., 2003] Tang, D., Yamamoto, H., and Dowell, E. (2003). Flutter and limit cycle oscillations of two-dimensional panels in three-dimensional axial flow. *Journal of Fluids and Structures*, 17(2):225–242.

[Tang et al., 2007] Tang, L., Paï , M. P., et al. (2007). On the instability and the post-critical behaviour of two-dimensional cantilevered flexible plates in axial flow. *Journal of Sound and Vibration*, 305(1-2):97–115.

[Tobalske, 2007] Tobalske, B. W. (2007). Biomechanics of bird flight. *Journal of Experimental Biology*, 210(18):3135–3146.

[Trimarchi et al., 1970] Trimarchi, D., Turnock, S., Chapelle, D., and Taunton, D. (1970). Fluid-structure interactions of anisotropic thin composite materials for application to sail aerodynamics of a yacht in waves.

[Virot et al., 2013] Virot, E., Amandolese, X., and Hémon, P. (2013). Fluttering flags: An experimental study of fluid forces. *Journal of fluids and structures*, 43:385–401.

[Watanabe et al., 2002] Watanabe, Y., Suzuki, S., Sugihara, M., and Sueoka, Y. (2002). An experimental study of paper flutter. *Journal of fluids and Structures*, 16(4):529–542.

[White, 2006] White, F. M. (2006). *Viscous fluid flow*, volume 3. McGraw-Hill New York.

[Yu and Liu, 2015] Yu, Y. and Liu, Y. (2015). Flapping dynamics of a piezoelectric membrane behind a circular cylinder. *Journal of Fluids and Structures*, 55:347–363.

[Yu and Liu, 2016] Yu, Y. and Liu, Y. (2016). Energy harvesting with two parallel pinned piezoelectric membranes in fluid flow. *Journal of Fluids and Structures*, 65:381–397.

[Yu et al., 2019] Yu, Y., Liu, Y., and Amandolese, X. (2019). A review on fluid-induced flag vibrations. *Applied Mechanics Reviews*, 71(1).

[Yu et al., 2017] Yu, Y., Liu, Y., and Chen, Y. (2017). Vortex dynamics behind a self-oscillating inverted flag placed in a channel flow: Time-resolved particle image velocimetry measurements. *Physics of Fluids*, 29(12):125104.

[Zhang et al., 2000] Zhang, J., Childress, S., Libchaber, A., and Shelley, M. (2000). Flexible filaments in a flowing soap film as a model for one-dimensional flags in a two-dimensional wind. *Nature*, 408(6814):835–839.

Appendix A: Tables of Data

The Tables A.1-A.3 contain all the values for Sample #1, Sample #2, and Sample #3. These values are for the fluttering cases of all the Re and measured non-dimensional values as well as key membrane characteristics. The cases that have been selected for in-depth study are also indicated. In the Table A.3, "Trans" indicates the Re at the membrane is going from a mode 2 flutter to a mode 3. On the same table, "CH" indicated that the membrane is in chaotic flutter in which several measurements aren't possible.

Table A.1: Table of non-dimensional values for Sample #1.

Index	Re	C_D	R_1	R_2	A_1 (mm)	$f(Hz)$	N_e (mm)	A_2 (mm)	Group
1	56k	0.070	2.77	14.4×10^{-3}	22.58	82.00	5.94	N/A	-
2	57k	0.115	2.77	13.9×10^{-3}	25.67	82.50	6.93	N/A	-
3	58k	0.131	2.77	13.4×10^{-3}	27.40	83.33	8.07	N/A	D
4	59k	0.150	2.77	12.9×10^{-3}	29.85	83.83	8.98	N/A	-
5	60k	0.169	2.77	12.4×10^{-3}	31.69	84.50	9.96	N/A	F
6	61k	0.187	2.77	11.9×10^{-3}	31.88	85.33	9.67	N/A	E
7	62k	0.204	2.77	11.5×10^{-3}	34.86	86.17	11.01	N/A	-
8	64k	0.216	2.77	11.1×10^{-3}	36.26	86.83	12.36	N/A	-
9	65k	0.228	2.77	10.7×10^{-3}	37.54	87.83	12.80	N/A	-
10	66k	0.239	2.77	10.3×10^{-3}	38.37	88.67	12.73	N/A	-
11	67k	0.252	2.77	10.0×10^{-3}	39.61	89.83	13.21	N/A	-
12	68k	0.260	2.77	9.7×10^{-3}	40.36	90.50	13.35	N/A	-
13	69k	0.267	2.77	9.3×10^{-3}	41.04	91.33	14.00	N/A	-
14	70k	N/A	2.77	9.1×10^{-3}	N/A	92.33	N/A	N/A	-
15	71k	N/A	2.77	8.8×10^{-3}	N/A	93.17	N/A	N/A	-
16	73k	N/A	2.77	8.5×10^{-3}	N/A	94.33	N/A	N/A	-
17	74k	N/A	2.77	8.2×10^{-3}	N/A	95.17	N/A	N/A	-
18	75k	N/A	2.77	8.0×10^{-3}	N/A	95.67	N/A	N/A	-

Table A.2: Table of non-dimensional values for Sample #2.

Index	Re	C_D	R_1	R_2	A_1 (mm)	$f(Hz)$	N_e (mm)	A_2 (mm)	Group
1	57k	0.016	2.14	9.0×10^{-3}	SS	SS	SS	N/A	-
2	53k	0.040	2.14	10.3×10^{-3}	22.00	45.63	5.89	N/A	-
3	54k	0.063	2.14	9.8×10^{-3}	28.24	46.25	7.25	N/A	-
4	57k	0.100	2.14	9.0×10^{-3}	36.71	48.13	10.02	N/A	-
5	59k	0.122	2.14	8.4×10^{-3}	40.92	49.38	11.52	N/A	-
6	61k	0.138	2.14	7.7×10^{-3}	43.80	51.25	12.52	N/A	D & E
7	64k	0.152	2.14	7.2×10^{-3}	46.03	52.50	13.92	N/A	-
8	66k	0.162	2.14	6.7×10^{-3}	47.54	53.75	13.75	N/A	-
9	68k	0.168	2.14	6.3×10^{-3}	48.54	54.63	15.40	N/A	F
10	70k	0.174	2.14	5.9×10^{-3}	49.72	55.63	16.36	N/A	-
11	73k	0.180	2.14	5.5×10^{-3}	50.86	57.50	16.18	N/A	-
12	75k	0.182	2.14	5.2×10^{-3}	51.47	58.75	17.30	N/A	-
13	77k	0.184	2.14	4.9×10^{-3}	52.00	59.38	16.80	N/A	-
14	80k	0.185	2.14	4.6×10^{-3}	52.70	60.63	18.55	N/A	-
15	82k	0.187	2.14	4.3×10^{-3}	53.13	62.50	18.89	N/A	C
16	84k	0.188	2.14	4.1×10^{-3}	N/A	N/A		N/A	-

Table A.3: Table of non-dimensional values for Sample #3.

Index	Re	C_D	R_1	R_2	A_1 (mm)	$f(Hz)$	N_e (mm)	A_2 (mm)	Group
1	44k	0.034	1.48	10.1×10^{-3}	32.6	20.25	8.5	N/A	-
2	48k	0.078	1.48	8.5×10^{-3}	47.44	22.13	13.78	N/A	A
3	51k	0.098	1.48	7.5×10^{-3}	54.18	22.63	17.12	N/A	-
4	55k	0.110	1.48	6.6×10^{-3}	57.95	23.75	21.09	N/A	-
5	58k	0.121	1.48	5.9×10^{-3}	61.63	24.75	22.60	N/A	-
6	61k	0.131	1.48	5.3×10^{-3}	64.04	25.75	24.95	N/A	D & E
7	64k	0.117	1.48	4.8×10^{-3}	60.66	27.38	21.14	N/A	-
8	68k	0.116	1.48	4.3×10^{-3}	60.88	28.63	21.08	N/A	-
9	71k	0.113	1.48	4.0×10^{-3}	58.74	30.25	18.76	N/A	-
10	74k	0.106	1.48	3.6×10^{-3}	56.46	31.63	18.38	N/A	-
11	77k	0.099	1.48	3.3×10^{-3}	53.46	34.00	16.03	N/A	-
12	81k	0.089	1.48	3.1×10^{-3}	59.22	35.25	18.63	Trans	-
13	84k	0.108	1.48	2.8×10^{-3}	45.33	49.13	16.16	3.03	C
14	87k	0.149	1.48	2.6×10^{-3}	49.93	53.13	18.14	4.03	-
15	90k	0.173	1.48	2.4×10^{-3}	51.25	55.88	18.90	3.83	F
16	93k	0.194	1.48	2.3×10^{-3}	54.71	58.75	19.25	4.24	-
17	97k	0.206	1.48	2.1×10^{-3}	59.70	60.63	22.53	4.35	-
18	100k	0.215	1.48	2.0×10^{-3}	60.18	62.25	22.45	4.66	-
19	103k	0.225	1.48	1.9×10^{-3}	65.96	N/A	23.60	5.05	B
20	106k	N/A	1.48	1.8×10^{-3}	CH	CH	CH	CH	-
21	110k	0.251	1.48	1.7×10^{-3}	CH	CH	CH	CH	-
22	113k	0.265	1.48	1.6×10^{-3}	CH	CH	CH	CH	-
23	116k	0.278	1.48	1.5×10^{-3}	CH	CH	CH	CH	-
24	119k	0.283	1.48	1.4×10^{-3}	CH	CH	CH	CH	-
25	123k	0.290	1.48	1.3×10^{-3}	CH	CH	CH	CH	-